The Astrophysical Journal, 892:95 (18pp), 2020 April 1 https://doi.org/10.3847/1538-4357/ab7a93

Numerical Modeling of Suprathermal Electron Transport in the Solar Wind: Effects of Whistler Turbulence

Bofeng Tang[1], Gary P. Zank[1,2], and Vladimir I. Kolobov[2,3]
[1] Department of Space Science, University of Alabama in Huntsville, Huntsville, AL 35899, USA
[2] Center for Space Plasma and Aeronomic Research (CSPAR), University of Alabama in Huntsville, Huntsville, AL 35899, USA
[3] CFD Research Corporation, Huntsville, AL 35806, USA
Received 2019 November 22; revised 2020 February 23; accepted 2020 February 25; published 2020 April 1

Abstract

The solar wind electron velocity distribution function deviates significantly from an equilibrium Maxwellian distribution and is composed of a Maxwellian core, a suprathermal halo, a field-aligned component strahl, and a higher-energy superhalo. Wave–particle interactions associated with whistler wave turbulence are introduced into the kinetic transport equation to describe the interaction between the suprathermal electrons and the whistler waves and to explain the observation that the halo and the strahl relative densities vary in an opposite sense. An efficient numerical method has been developed to solve the Fokker–Planck kinetic transport equation. Application of the numerical method to suprathermal electrons in the solar wind in the presence of whistler waves is presented. Comparison and analysis between the numerical results and observations are made.

Unified Astronomy Thesaurus concepts: Solar wind (1534)

1. Introduction

The Sun constantly emits a flux of electrically charged particles into space, primarily protons and electrons, known as the solar wind. The solar wind flow is supersonic with respect to the protons and subsonic with respect to the electrons. Observations show that the velocity distribution function (VDF) of both electrons and protons in the solar wind deviates significantly from a thermal equilibrium form and exhibits an enhanced suprathermal tail (Feldman et al. 1974; Feldman et al. 1975; Marsch et al. 1982). In particular, the solar wind electron VDF can be modeled as being composed of three or four components: the Maxwellian "core," a suprathermal "halo," a field-aligned "strahl," and a very high energy "superhalo" (Ergun et al. 1998; Wang et al. 2012). The word "suprathermal" means the combination of the last three components (halo, strahl, and superhalo). The Maxwellian core is characterized by energies of $<\sim$10 eV, the halo and strahl fall in the energy range of about 10^2–10^3 eV, and the superhalo lies in the range of 10^3–10^5 eV. All four components are distinguishable from each other by the shape of their velocity space distribution functions. The Maxwellian core, halo, and superhalo populations are observed to be relatively isotropic compared to the strahl, which is highly field aligned to the ambient magnetic field. Observations at 1 au generally show that the Maxwellian component composes about 95% of the total electron number density, the halo approximately 4%, and the strahl the remaining 1%. The number density of the superhalo component relative to the core is extremely low and only on the order of less than 10^{-6}. Although suprathermal electrons compose a tiny fraction of the total electron number density, they are responsible for most of the heat flux transported away from the Sun owing to their high energy (Štverák et al. 2009) and are important to the solar wind dynamics.

Observations of the solar wind electron distribution have been made for decades, and two fitting models are currently invoked in observations and theory. In the first method a single kappa distribution is used as a global model to fit the entire electron velocity distribution, while in the second method the entire electron velocity distribution is divided into more than two parts and each component is fitted by a Maxwellian distribution or an individual kappa distribution. The first method is called the global kappa model, and the second is called the dual Maxwellian-kappa model. The global kappa distribution fitting model needs a reduced number of parameters and is easy to manipulate (Pierrard & Lazar 2010). However, a dual Maxwellian-kappa approach is more accurate to fit the observed distribution than the global kappa (Lazar et al. 2017). Besides, a dual Maxwellian-kappa model can describe any slow or fast solar condition at large heliocentric distances (Maksimovic et al. 2005), or a condition in which the relative density of the strahl is negligibly low (Lazar et al. 2014). Third, in the dual Maxwellian-kappa model, these distinct components may have different origins (Pierrard et al. 1999; Maksimovic et al. 2005). Therefore, Lazar et al. (2017) suggested that the best-fitting model should contain three components: a Maxwellian core, a kappa halo, and a drifting-kappa strahl.

Data analyses of the radial evolution of the electron VDF from 0.3 to 4 au found that with increasing heliocentric distance the relative number density (to the total number density) of strahl electrons decreases and the relative number density of halo electrons increases, while the relative number density of the core remains unchanged (Maksimovic et al. 2005; Štverák et al. 2009; Tao et al. 2016). That the halo and the strahl relative densities vary in an opposite sense, as well as the fact that they both lie in the same energy range (10^2–10^3 eV), suggests that the halo and strahl electrons are the same and that the strahl electrons are pitch-angle scattered into the halo by some mechanism such as Coulomb collisions or by pitch-angle scattering by plasma waves as they propagate away from the corona (Horaites et al. 2015; Kim et al. 2015).

Suprathermal (halo, strahl, and superhalo) electrons are generally thought to originate in the solar corona (Pierrard et al. 1999; Štverák et al. 2008; Che & Goldstein 2014) and to propagate away from the Sun along interplanetary magnetic field lines. The strahl can be observed in either the parallel or antiparallel magnetic field direction, or sometimes even in both

directions in certain circumstances (Pilipp et al. 1987a; Anderson et al. 2012). If the propagation were purely adiabatic, the suprathermal electrons would be focused into a narrow beam ($<1^\circ$ at 1 au) owing to magnetic moment conservation as the magnetic field strength weakens with heliodistance from the Sun. However, observations show that the pitch-angle width of the strahl is broader than it would be for an adiabatic expanding model (Lemons & Feldman 1983). *Helios-1* observations from 0.3 to 1 au showed strahl widths from 5° to 60° (Pilipp et al. 1987a, 1987b). The pitch-angle width of the strahl electrons increases on average as the electron energy increases (Pagel et al. 2007) and is observed to broaden with radial distance from the Sun (Hammond et al. 1996). That strahl electrons have a finite width may be a consequence of competition between magnetic focusing as the interplanetary magnetic field weakens with heliodistance from the Sun and particle scattering acting to broaden the strahl electrons as they propagate from the Sun. It is therefore reasonable to assume that the suprathermal electrons as a whole originate in the corona as a strahl and propagate into the interplanetary medium, where they are scattered from the strahl into a halo distribution (Lie-Svendsen et al. 1997; Pierrard et al. 2011; Kim et al. 2015; Graham et al. 2017; Horaites et al. 2017). A solar wind population, sometimes called a proto-halo, has been observed and is thought to be part of the formation of the halo from the scattering of the strahl (Gurgiolo et al. 2012; Gurgiolo & Goldstein 2016).

Various theories have tried to address the possible mechanism that forms these suprathermal components in the solar wind. Coulomb collisions between charged particles were first considered as a possible mechanism to scatter supathermal electrons propagating in interplanetary space. Lie-Svendsen & Rees (1996) derived an analytical solution of the kinetic electron transport equation for an electron–electron Coulomb collision term. Lie-Svendsen et al. (1997) applied their method to the high-speed solar wind. In their model, the large-scale electric field, density, and temperature are self-consistently computed from fluid models. Lie-Svendsen & Leer (2000) later added electron–proton scattering into their equation to investigate the role of protons. They found that electron–electron collisions dominate electron–proton collisions in the formation of a high-energy tail of solar wind electrons. By employing a different and reasonable boundary condition, Pierrard et al. (1999, 2001) also considered the effect of electron–electron and electron–proton Coulomb collisions on the electron velocity distribution in the corona. Salem et al. (2003) show that the electron temperature anisotropy appears to depend mainly on Coulomb collisions. They also show that the role of Coulomb collisions in regulating the electron heat flux is not as negligible as has been suggested by other authors. Obviously, a higher collision rate ensures that the distribution function becomes more isotropized and the heat flux in reduced. Landi et al. (2012) solved a fully kinetic model of the solar wind including Coulomb collisions and spherical expansion and showed that the combined effects of expansion and Coulomb collisions lead to the formation of two populations: a collision-dominated cold and dense population that is almost isotropic in velocity space (the halo) and a weakly collisional, tenuous field-aligned and antisunward-drifting population (the strahl). Horaites et al. (2015, 2017) considered the effect of Coulomb collisions among electrons and developed an analytic model of solar wind electron kinetics that yielded a simple expression for the shape of the strahl distribution. Their work supports the possibility that Coulomb collisions are an important source of pitch-angle scattering and suggests that other physical effects are needed for improving their strahl scattering model. However, their model applies only for relatively low energy particles with energy $\leqslant 200$ eV. For electron energies $\geqslant 200$ eV their theory indicates that the scattering provided by Coulomb collisions alone is insufficient (Horaites et al. 2018).

In the high-energy range (1 keV) and at large heliocentric distances (above about 10 solar radii) where the electron number density is dilute, Coulomb collisions are too weak to scatter suprathermal electrons efficiently. Numerical simulations show that Coulomb collisions alone cannot scatter the suprathermal electrons into the observed width (Vocks et al. 2005; Pagel et al. 2007; Pierrard et al. 2011). It is necessary to include other scattering mechanisms, such as wave–particle interactions. Vocks & Mann (2003) and Vocks et al. (2005) studied the formation of the halo and strahl in the electron VDF in the solar corona and solar wind due to whistler turbulence wave–particle interactions for electron energies below 1 keV. Vocks et al. (2008) extended their results to electron energies of more than 100 keV. Their studies show that the quiet solar corona is capable of producing suprathermal electron VDFs by whistler turbulence wave–particle interactions and asserted that such an electron population should be present in the solar wind. On the other hand, Pierrard et al. (2011) extended the exospheric model of Maksimovic et al. (1997) by adding a diffusion coefficient term derived from wave–particle interactions associated with whistler wave turbulence that has a different form than that of Vocks et al. (2005). Pierrard et al. (2011) found that the nonthermal tails in the solar wind electron VDF emerge from an initially Maxwellian distribution function by wave–particle interactions associated with whistler wave turbulence.

Previous theories treat the entire multicomponent solar wind electron VDF as a whole. In prior models, all solar wind electrons are subjected to these scattering mechanisms collectively as they propagate from the Sun. Much of the focus of prior models was on the acceleration of the Maxwellian core electrons to form nonthermal high-energy tails in the solar wind VDFs. However, Kim et al. (2015) and Yoon et al. (2015) proposed an asymptotic scattering theory for solar wind electrons in local equilibrium with plasma wave turbulence by assuming that the local solar wind electron VDF is a superposition of a Maxwellian core, halo, and superhalo. In their model the Maxwellian core does not experience any collisionless scattering, and the halo electrons only interact with whistler wave turbulence, and superhalo electrons only with Langmuir wave turbulence. On multiplying by an arbitrary constant as large as 10^7 to the model VDF, their results were comparable to observations at 1 au (Yoon et al. 2013). Recently, Boldyrev & Horaites (2019) developed a kinetic theory for the electron strahl scattered by both Coulomb collisions and wave–particle interactions associated with whistler turbulence. However, the difference between the present approach and that of Boldyrev & Horaites (2019) is that their diffusion terms in the drift-kinetic equation only include pitch-angle scattering associated with Coulomb collisions and whistler wave–particle interactions, whereas we include both scattering in pitch angle and diffusion in velocity space for suprathermal electrons experiencing whistler

wave–particle interactions. We will see later that diffusion in velocity space, although small compared with scattering in pitch angle, plays an important role in the kinetic equation and the transport of suprathermal electron VDF.

In the present paper, we introduce a wave–particle interaction term into the kinetic transport equation that describes the interaction of only suprathermal electrons with whistler wave turbulence. We developed a numerical method using adaptive mesh refinement to solve an advection-diffusion-like Fokker–Planck kinetic equation in 3D phase space. This numerical method is used to investigate the effects of resonant wave–particle interactions on the suprathermal component of the solar wind electron VDF. By studying the temporal and radial evolution of the suprathermal electron, we show that resonant wave–particle interactions associated with whistler turbulence can significantly pitch-angle scatter an initially highly anisotropic field-aligned suprathermal electron VDF injected at an inner boundary into a nearly isotropic distribution at 1 au. In the last part of the present paper we compare our calculated solar wind electron VDFs with observations and show that they are indeed very comparable, which supports the validity of our assumptions and methods.

The structure of the present paper is as follows. Section 2 provides an overview of the transport model of suprathermal electrons and the numerical method. The method of characteristics and the analytic solution to the kinetic transport equation when diffusion is ignored are also discussed in this section. Section 3 presents some results of the numerical method. Section 4 contains a discussion about the calculated electron VDF and corresponding macroparameters. The summary and conclusions are given in Section 5.

2. Model Equations and the Numerical Method

Here we present a kinetic equation describing the transport of suprathermal electrons in an expanding solar wind background. We first assume that the total electron VDF that originates in the corona is composed of two main parts: a Maxwellian core population (labeled by the subscript c) and a suprathermal part (labeled by the subscript s). It is unclear whether the Maxwellian core electrons experience wave–particle interactions in the supersonic solar wind. Presumably, Coulomb collisions in the low corona and below ensure a Maxwellian energy distribution of core electrons. It has been suggested that ion acoustic modes may scatter low-energy electrons in the solar wind itself, but this remains largely conjectural (Marsch et al. 1982). For the present, we simply assume that a core Maxwellian distribution exists, that its associated electrons do not experience any scattering by whistler waves, and that it is maintained throughout the supersonic solar wind (Kim et al. 2015). We then follow the evolution of a suprathermal electron population only. Although the suprathermal electrons f_s are considered as a minor species in the background Maxwellian core, the suprathermal component carries the heat flux. In our work the VDF is measured in the frame of reference of the solar wind bulk velocity. The total electron VDF at a given position is the combination of the corresponding Maxwellian core f_c and the calculated suprathermal f_s at that position. Although we do not discuss it further here, the inclusion of the core Maxwellian distribution will be incorporated in future work in the following way. As we discuss below, suprathermal electrons can be scattered by whistler turbulence. We will assume a Maxwellian distribution for core electrons at the inner boundary and further assume that only fast electrons that satisfy $U \geqslant v_s \approx v_{\rm whistler}$ will experience scattering by whistler turbulence. All electrons will be simultaneously subjected to Coulomb scattering. Such a future simulation will allow us to understand to what extent the Maxwellian core is preserved with increasing heliocentric distance and whether electron runaway will result in the formation of the electron strahl. For the present, however, we focus exclusively on the evolution of an initially anisotropic distribution of suprathermal electrons. Since the heat flux of a Maxwellian velocity distribution is zero, the heat flux of the total electron distribution is just the heat flux of the suprathermal component, which we will evaluate.

The general kinetic transport equation for the evolution of the VDF $f(\boldsymbol{x}, \boldsymbol{v}, t)$ of nonrelativistic electrons in the inertial frame is

$$\frac{\partial f}{\partial t} + \boldsymbol{v}\cdot\nabla f + \frac{\boldsymbol{F}}{m}\cdot\nabla_{\boldsymbol{v}} f = \left(\frac{\delta f}{\delta t}\right)_{\rm sc}, \tag{1}$$

where $\boldsymbol{F} = q/c(\boldsymbol{E} + \boldsymbol{v}\times\boldsymbol{B})$ is the force acting on the particle, m the particle mass, and $(\delta f/\delta t)_{\rm sc}$ the scattering term, which should include Coulomb collisions, wave–particle interactions, and any other possible scattering mechanisms. The acceleration of electrons by gravity is negligible compared to the Lorentz force acting on electrons ($|e\boldsymbol{E}/m\boldsymbol{g}| \gg 1$) over the distance ($r > 0.1$ au) that we consider for electron transport in its supersonic solar wind. Consider a frame of reference that propagates in the inertial "rest" frame at a velocity $\boldsymbol{U}$, such as the solar wind frame, and rewrite Equation (1) in mixed coordinates $(\boldsymbol{x}, \boldsymbol{v}, t)$, where $\boldsymbol{v}$ is the velocity variable measured in the reference frame moving with $\boldsymbol{U}$, and $\boldsymbol{x}$ is the position in the inertial frame (Isenberg 1997). Since the electron gyroperiod is much smaller than any other characteristic timescale, it is reasonable to assume gyrotropy of the electron distribution. We write the electron VDF in a spherical coordinates system in velocity space and average Equation (1) over gyrophase (Skilling 1971; Zank 2014):

$$\begin{aligned}
&\frac{\partial f}{\partial t} + (v\mu\boldsymbol{b} + \boldsymbol{U})\cdot\nabla f \\
&+\left[\left(-\frac{\partial \boldsymbol{U}}{\partial t} - \boldsymbol{U}\cdot\frac{\partial \boldsymbol{U}}{\partial \boldsymbol{x}}\right)\cdot\boldsymbol{b}\frac{\mu}{v} - \frac{1-\mu^2}{2}\nabla\cdot\boldsymbol{U}\right. \\
&\left.-\frac{3\mu^2-1}{2}\boldsymbol{b}\cdot\frac{\partial \boldsymbol{U}}{\partial \boldsymbol{x}}\cdot\boldsymbol{b} + \frac{qE_{\parallel}\mu}{mv}\right]v\frac{\partial f}{\partial v} \\
&+\frac{1-\mu^2}{2}\left[v\nabla\cdot\boldsymbol{b} + \mu\nabla\cdot\boldsymbol{U} - \left(\frac{\partial \boldsymbol{U}}{\partial t} + \boldsymbol{U}\cdot\frac{\partial \boldsymbol{U}}{\partial \boldsymbol{x}}\right)\right. \\
&\left.\cdot\boldsymbol{b}\frac{2}{v} - 3\mu\boldsymbol{b}\cdot\frac{\partial \boldsymbol{U}}{\partial \boldsymbol{x}}\cdot\boldsymbol{b} + \frac{2qE_{\parallel}}{mv}\right]\frac{\partial f}{\partial \mu} \\
&= \left(\frac{\delta f}{\delta t}\right)_{\rm sc},
\end{aligned} \tag{2}$$

where $\boldsymbol{b} \equiv \boldsymbol{B}/|\boldsymbol{B}|$ is the unit vector along the large-scale magnetic field, $E_{\parallel}$ the electric field component parallel to the ambient magnetic field, v the magnitude of electron velocity, and μ the cosine of pitch angle: $\mu = \cos\theta$.

Consider a constant radial flow with $\boldsymbol{U} = U\hat{e}_r$ and a large-scale radial magnetic field pointing away from the Sun, $\boldsymbol{b} = \hat{e}_r$.

This assumption of a radial magnetic field is simple and is reasonably valid up to 1 au (Pierrard et al. 1999). Moreover, it has been shown that a more realistic spiral magnetic field may change the temperature anisotropies but does not significantly change the heliocentric distribution of other parameters of the solar wind (Chen et al. 1972; Pierrard et al. 2001). Then, the gyrophase-averaged kinetic equation for nonrelativistic suprathermal electrons with VDF $f(r, v, \mu)$ in the solar wind frame has the form

$$\frac{df}{dt} + (\mu v + U)\frac{\partial f}{\partial r} - \frac{1-\mu^2}{r}Uv\frac{\partial f}{\partial v} + \frac{1-\mu^2}{r}(v+\mu U)\frac{\partial f}{\partial \mu} + \frac{qE_\parallel}{m}\mu\frac{\partial f}{\partial v} + \frac{qE_\parallel}{m}\frac{(1-\mu^2)}{v}\frac{\partial f}{\partial \mu} = \left(\frac{\delta f}{\delta t}\right)_{\rm sc}, \tag{3}$$

where r is the radial distance. In the solar wind, the velocity of suprathermal electrons v is always much larger than the velocity of the solar wind U, i.e., $v \gg U$, making it safe to ignore U. The gyrophase-averaged kinetic transport equation is then further simplified as

$$\frac{\partial f}{\partial t} + \mu v\frac{\partial f}{\partial r} + \left[\frac{v(1-\mu^2)}{r} - \frac{eE_\parallel}{m}\frac{1-\mu^2}{v}\right] \times \frac{\partial f}{\partial \mu} - \frac{eE_\parallel}{m}\mu\frac{\partial f}{\partial v} = \left(\frac{\delta f}{\delta t}\right)_{\rm sc}. \tag{4}$$

The above equation resembles the kinetic equation used by Pierrard et al. (2011) but is different from that used by other authors (such as Shalchi 2011; Horaites et al. 2015, Boldyrev & Horaites 2019). This is because we and Pierrard et al. (2011) assume that the magnetic field is radial and hence has the adiabatic focusing term $v(1-\mu^2)/r$ in the spherically expanding magnetic field (Isenberg 1997). Other authors do not use such a simple magnetic field and typically use the form $\sim\partial \ln B/\partial x$, or equally $\sim(1/B)\,\partial B/\partial x$, to describe the interplanetary magnetic field variation, where x is the distance along the magnetic field line. Lie-Svendsen & Rees (1996) provided a derivation of the adiabatic focusing term using a method of azimuthal averaging which is exactly the same method as our method of gyrophase averaging. It is easy to show that the terms $\sim\partial \ln B/\partial x$ assume the form $\sim 1/x$ if a monopole magnetic field is assumed. From the term $\nabla \cdot \boldsymbol{b}$ in Equation (2), it is apparent that only the direction of magnetic field (i.e., $\boldsymbol{b}$) affects the magnetic force in the kinetic equation and the transport of particles.

The thermal electron distribution is not sufficiently energetic to experience scattering by whistler waves. We assume that the core thermal electron distribution is and remains Maxwellian throughout the supersonic solar wind. We prescribe a simple set of radial profiles that describe how the basic bulk electron plasma parameters evolve. Equation (4) describes only the transport of those electrons that scatter resonantly with whistler waves. For simplicity of notation we will drop the subscript s from the distribution function. Keep in mind that all the following kinetic equations are only for suprathermal electrons and the distribution function f is actually f_s.

2.1. Wave–Particle Interactions due to Whistler Wave Turbulence

Here we consider only one scattering mechanism for the suprathermal electron VDF in the solar wind, namely, wave–particle interactions due to whistler wave turbulence, since in the high-energy range and at large heliocentric distances Coulomb collisions are too weak to scatter suprathermal electrons efficiently. This means that the suprathermal electrons resonate only with whistler wave turbulence when propagating from the Sun (Kim et al. 2015; Yoon 2015). Fujimoto & Sydora (2008) showed that whistler waves are driven by the electron temperature anisotropy in the downstream region of the electron outflow and are generated as a result of magnetic reconnection processes, which is consistent with *Cluster* observations of Wei et al. (2007). Tong et al. (2019) provided a statistical survey of whistler waves in the solar wind at 1 au using *Artemis* observations, identifying various important properties of whistler waves.

The scattering term hence becomes

$$\left(\frac{\delta f}{\delta t}\right)_{\rm sc} = \left(\frac{\delta f}{\delta t}\right)_{\rm wp}.$$

In the gyrophase-averaged kinetic transport Equation (4), the term that describes the scattering of the electron distribution in the presence of whistler waves is chosen to be of the form (Schlickeiser 1989)

$$\left(\frac{\delta f}{\delta t}\right)_{\rm wp} = \frac{\partial}{\partial \mu}\left(D_{\mu\mu}\frac{\partial f}{\partial \mu}\right) + \frac{1}{v^2}\frac{\partial}{\partial v}\left(\frac{v^2}{m^2}D_{vv}\frac{\partial f}{\partial v}\right) + \frac{\partial}{\partial \mu}\left(\frac{1}{m}D_{\mu v}\frac{\partial f}{\partial v}\right) + \frac{1}{v^2}\frac{\partial}{\partial v}\left(\frac{v^2}{m}D_{v\mu}\frac{\partial f}{\partial \mu}\right). \tag{5}$$

From Steinacker & Miller (1992) and Pierrard et al. (2011), the whistler wave–particle interaction tensor in the case of nonrelativistic electrons has the form

$$D_{vv} = \frac{\Omega_e m^2 c^2 \pi}{3}\frac{A}{a}\left(\frac{\beta|\mu|}{a}\right)^{\frac{s-1}{3}}; \tag{6a}$$

$$D_{\mu v} = D_{v\mu} = -\frac{\Omega_e mc\pi}{3}\frac{A}{a}\left[\frac{\mu}{|\mu|}\left(\frac{\beta|\mu|}{a}\right)^{\frac{s-2}{3}} + \frac{\mu}{\beta}\left(\frac{\beta|\mu|}{a}\right)^{\frac{s-1}{3}}\right] \times (1-\mu^2); \tag{6b}$$

$$D_{\mu\mu} = \frac{\Omega_e \pi}{3}\frac{A}{a}\left[\left(\frac{\beta|\mu|}{a}\right)^{\frac{s-3}{3}} + \frac{2\mu}{\beta}\frac{\mu}{|\mu|}\left(\frac{\beta|\mu|}{a}\right)^{\frac{s-2}{3}} + \left(\frac{\mu}{\beta}\right)^2\left(\frac{\beta|\mu|}{a}\right)^{\frac{s-1}{3}}\right](1-\mu^2), \tag{6c}$$

where $\beta = v/c$, $a = \Omega_e^2/\omega_{pe}^2$. The normalization constant $A = 0.1$, and the spectral index of whistler waves is in the interval $s = 3/2 \sim 2$.

In the derivation of these diffusion coefficients, Steinacker & Miller (1992) assumed that the whistler spectral densities have equal intensities in both propagation directions and only considered a very simple spectral density with a power law. All these assumptions result in much larger diffusion coefficient values than appear to be appropriate to realistic

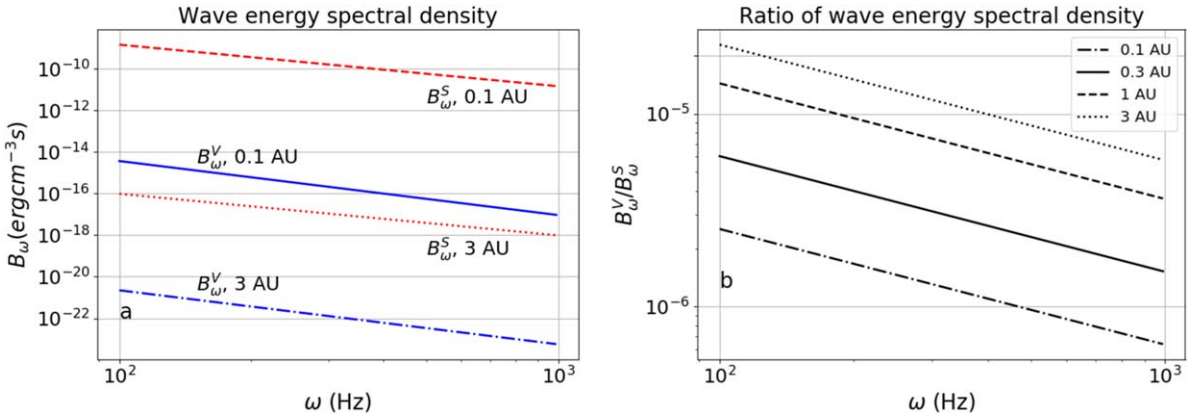

Figure 1. Energy spectral densities as a function of wave frequency ω. (a) Comparison of the energy spectral densities from Vocks & Mann (2003) and Steinacker & Miller (1992) at 0.1 and 3 au. (b) Ratio of energy spectral density between Vocks & Mann (2003) and Steinacker & Miller (1992) at 0.1, 0.3, 1, and 3 au.

solar wind conditions. In our calculations we also found that their diffusion coefficients are so extremely large that unrealistic electron transport results arise. On the other hand, Vocks & Mann (2003) and Vocks et al. (2005) obtained a different whistler wave turbulence diffusion coefficient by choosing a different expression for the energy spectral density of whistler wave turbulence based on solar wind measurements obtained by Salem (2000). The observational energy spectrum density of whistler wave turbulence given by Salem (2000) is thus more realistic than that assumed by Steinacker & Miller (1992). Figure 1 shows a comparison between energy spectral densities of whistler wave turbulence from Vocks & Mann (2003) B^V_ω and Steinacker & Miller (1992) B^S_ω as a function of wave frequency ω, where the speed of solar wind was chosen as $U = 400$ km s^{-1} at 0.3 and 1 au separately. It is clear that B^S_ω is much larger, by a factor of about 10^6, than B^V_ω. This means that the diffusion coefficients (6) based on the Steinacker & Miller (1992) spectral B^S_ω are much larger than realistic values derived from solar wind data, which are calculated based on the assumed energy spectral density of the Vocks & Mann (2003) and Vocks et al. (2005) B^V_ω. Therefore, in order to use the diffusion coefficients (6) in our calculation, we multiply them by a small constant fraction f_r, which is an artificial manner to reduce them to smaller but possibly more realistic values. Since B^V_ω was obtained from observational measurements, we use this as a reference to estimate diffusion coefficients (6) that are close to their realistic values in the solar wind by adjusting the value of the fraction constant f_r. The possible and reasonable range of values for the fraction constant f_r depends on the ratio of the energy spectral density whistler wave turbulence used by Vocks & Mann (2003) to the energy spectral density whistler wave turbulence used by Steinacker & Miller (1992), i.e., B^V_ω/B^S_ω, at particular heliocentric distances. Figure 1(b) illustrates the values of B^V_ω/B^S_ω as a function of wave frequency ω at different heliocentric distances. It is clear that the fraction constant should be very small, and the value ranges from $\sim 10^{-6}$ to $\sim 10^{-4}$. In the following calculation, we choose the fraction constant to be $f_r = 2.5 \times 10^{-5}$ for case 1 and $f_r = 1 \times 10^{-5}$ for case 2.

2.2. Expanding Solar Wind Background

The radially expanding background magnetic field was chosen to have the form of Adhikari et al. (2017), which was adapted from Weber & Davis (1967),

$$B(r) = B_a\left(\frac{r_a}{r}\right)^2\left\{1+\left(\frac{\omega_a r}{U}\right)^2\left[1-\left(\frac{r_a}{r}\right)^2\right]^2\right\}^{1/2}, \quad (7)$$

where r is in units of au, $r_a \sim 0.05$ au, $\omega_a = 2.9 \times 10^{-6}$ rad s^{-1}, $U = 400$ km s^{-1}, and $B_a = 2.08 \times 10^3$ nT, so that $B(r = 1) = 0.45$ nT is the magnetic field at 1 au. Note that the exact value of the magnetic field does not affect the form of the transport kinetic equation, but rather affects the diffusion coefficients (6) because of the electron plasma frequency ω_{pe}. The number density of suprathermal electrons is much smaller than that of the Maxwellian core, which allows them to be treated as test particles. Their transport and radial evolution do not affect the radial profile of the Maxwellian core electrons. Moreover, we assume that the electron Maxwellian core exists and is maintained throughout the solar wind and forms a prescribed background. In the present paper we use simple radial profiles to represent the prescribed background Maxwellian core. Hence, other background Maxwellian core plasma parameters used to represent the expanding solar wind plasma are adopted from Horaites et al. (2015, 2017):

$$n_c = n_{c0} r^{-2}; \quad (8)$$

$$T_c = T_{c0} r^{-0.4}; \quad (9)$$

$$E_\parallel = 2.2\frac{T_{c0}k_B}{eR}r^{-1.4}, \quad (10)$$

where n_{c0} and T_{c0} are the Maxwellian core electron number density and temperature at 1 au, respectively, r is in units of au, and k_B is the Boltzmann constant.

2.3. Numerical Method of Solution of the Fokker–Planck Equation

We developed a numerical method to solve the Fokker–Plank kinetic equation using a finite-volume discretization with an octree Cartesian mesh, without splitting physical and velocity space (Kolobov et al. 2019). We adopted the Basilisk[4] framework for the solution of partial differential equations on adaptive Cartesian meshes (Tang et al. 2018). Details of the numerical method for solving kinetic equations are presented

[4] http://basilisk.fr

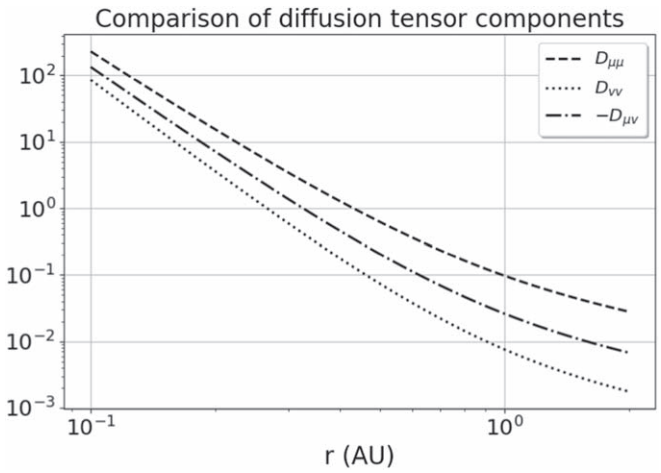

Figure 2. Comparison between the normalized components of the diffusion tensor when the constant fraction f_r was chosen to be 2.5×10^{-5}, $s = 2$, and $\mu = 0.9$.

by Kolobov (2003, 2013), Kolobov & Arslanbekov (2012), Arslanbekov et al. (2013), Zabelok et al. (2015), and Kolobov & Godyak (2019). We use Basilisk in a 3D Cartesian coordinates system to solve an advection-diffusion-like equation that has the form

$$\frac{\partial f}{\partial t} + \nabla \cdot (\boldsymbol{V} f) = \nabla \cdot (\mathbb{D} \cdot \nabla f), \tag{11}$$

where $f(x_1, x_2, x_3)$ is any general function, $\boldsymbol{V} = (V_1, V_2, V_3)$ the phase-space advection velocity vector, and $\mathbb{D}$ the phase-space diffusion tensor. Figure 2 shows a comparison between the three diffusion coefficients with an arbitrary choice of the constant f_r. It is clear that $D_{\mu\mu}$ is the largest, making pitch-angle scattering the most important of the wave–particle interactions due to whistler wave turbulence. $D_{\mu v}$, although larger than D_{vv}, is almost five times smaller than $D_{\mu\mu}$. This suggests that the kinetic transport equation for suprathermal electrons is dominated by the diagonal diffusion terms. In the present paper, we ignore the off-diagonal terms ($D_{\mu v}$ and $D_{v\mu}$) in the wave–particle interaction when we combine Equations (4), (5), and (6). Although D_{vv} is even smaller than $D_{v\mu}$, it introduces an important physical effect of diffusion and energization of electrons in velocity space and will be included in our code. Effects of off-diagonal diffusion will be investigated in a subsequent paper. Accordingly, the gyrophase-averaged kinetic transport equation for the VDF of suprathermal electrons in the solar wind that we solve has the form

$$\begin{aligned}\frac{\partial f}{\partial t} + \mu v \frac{\partial f}{\partial r} + \left[\frac{v(1-\mu^2)}{r} - \frac{eE_\parallel}{m}\frac{1-\mu^2}{v}\right]\frac{\partial f}{\partial \mu} \\ - \frac{eE_\parallel}{m}\mu\frac{\partial f}{\partial v} \\ = \frac{\partial}{\partial \mu}\left(D_{\mu\mu}\frac{\partial f}{\partial \mu}\right) + \frac{1}{v^2}\frac{\partial}{\partial v}\left(v^2 D_{vv}\frac{\partial f}{\partial v}\right).\end{aligned} \tag{12}$$

Both the pitch-angle scattering $D_{\mu\mu}$ and the velocity diffusion D_{vv} terms are included.

Introducing $f = Y/v^2 r^2$, we rewrite Equation (12) in conservation form to obtain an advection-diffusion-like equation for the function $Y = Y(r, v, \mu)$ in the 3D phase space,

$$\begin{aligned}&\frac{\partial Y}{\partial t} + \frac{\partial}{\partial r}(\mu v Y) + \frac{\partial}{\partial \mu}\left\{\left[\frac{v(1-\mu^2)}{r} - \frac{eE_\parallel}{m}\frac{1-\mu^2}{v}\right]Y\right\} \\ &+ \frac{\partial}{\partial v}\left\{\left[-\frac{eE_\parallel}{m}\mu + f_r\frac{\pi c^2}{15v}\frac{\Omega_e^3}{\omega_{pe}^2}\left(\frac{v}{c}\frac{\Omega_e^2}{\omega_{pe}^2}\right)^{\frac{s-1}{3}}|\mu|^{\frac{s-1}{3}}(1-\mu^2)\right]Y\right\} \\ &= \frac{\partial}{\partial v}\left[f_r\frac{\pi c^2}{30}\frac{\Omega_e^3}{\omega_{pe}^2}\left(\frac{v}{c}\frac{\Omega_e^2}{\omega_{pe}^2}\right)^{\frac{s-1}{3}}|\mu|^{\frac{s-1}{3}}(1-\mu^2)\frac{\partial Y}{\partial v}\right] \\ &+ \frac{\partial}{\partial \mu}\left\{f_r\frac{\pi}{30}\frac{\Omega_e^3}{\omega_{pe}^2}(1-\mu^2)\left[\left(\frac{v}{c}\frac{\Omega_e^2}{\omega_{pe}^2}\right)^{\frac{s-3}{3}}|\mu|^{\frac{s-3}{3}}\right.\right. \\ &\left.\left.+ 2\mu^2\frac{c}{v}\left(\frac{v}{c}\frac{\Omega_e^2}{\omega_{pe}^2}\right)^{\frac{s-2}{3}}|\mu|^{\frac{s-5}{3}} + \mu^2\frac{c^2}{v^2}\left(\frac{v}{c}\frac{\Omega_e^2}{\omega_{pe}^2}\right)^{\frac{s-1}{3}}|\mu|^{\frac{s-1}{3}}\right]\frac{\partial Y}{\partial \mu}\right\}.\end{aligned} \tag{13}$$

This kinetic transport equation for Y, which resembles Equation (11), describes the evolution of the suprathermal electron distribution function in 3D phase space and can be solved numerically. The spectral index of whistler waves s is in the interval $s = 3/2 \sim 2$. A larger spectral index yields smaller diffusion coefficients. In the present paper we choose $s = 2$ to keep the diffusion coefficients smaller.

2.4. Method of Characteristics and Analytic Solution

The kinetic Equation (12) without diffusion terms can be solved analytically by the method of characteristics. If we neglect the diffusion terms in Equation (13), the characteristic equations for the particle trajectories are given by

$$\frac{dr}{dt} = \mu v; \tag{14a}$$

$$\frac{dv}{dt} = -\frac{eE_\parallel}{m}\mu + f_r\frac{\pi c^2}{15v}\frac{\Omega_e^3}{\omega_{pe}^2}\left(\frac{v}{c}\frac{\Omega_e^2}{\omega_{pe}^2}\right)^{\frac{s-1}{3}}|\mu|^{\frac{s-1}{3}}(1-\mu^2); \tag{14b}$$

$$\frac{d\mu}{dt} = \frac{v(1-\mu^2)}{r} - \frac{eE_\parallel}{m}\frac{1-\mu^2}{v}. \tag{14c}$$

Terms with $E_\parallel$ are associated with the effect of the electric field parallel to the interplanetary magnetic field and describe the deceleration of electrons. Whistler wave–particle interactions (the term of f_r) result in acceleration of electrons. The term $v(1-\mu^2)/r$ comes from the gyrophase averaging process of the large-scale radial magnetic field pointing away from the Sun $\boldsymbol{b} = \hat{e}_r$. Lie-Svendsen & Rees (1996) showed that for a monopole magnetic field, the adiabatic focusing of the magnetic field on magnetized charged particles is completely equivalent to the effect of spherical geometry on neutral particles.

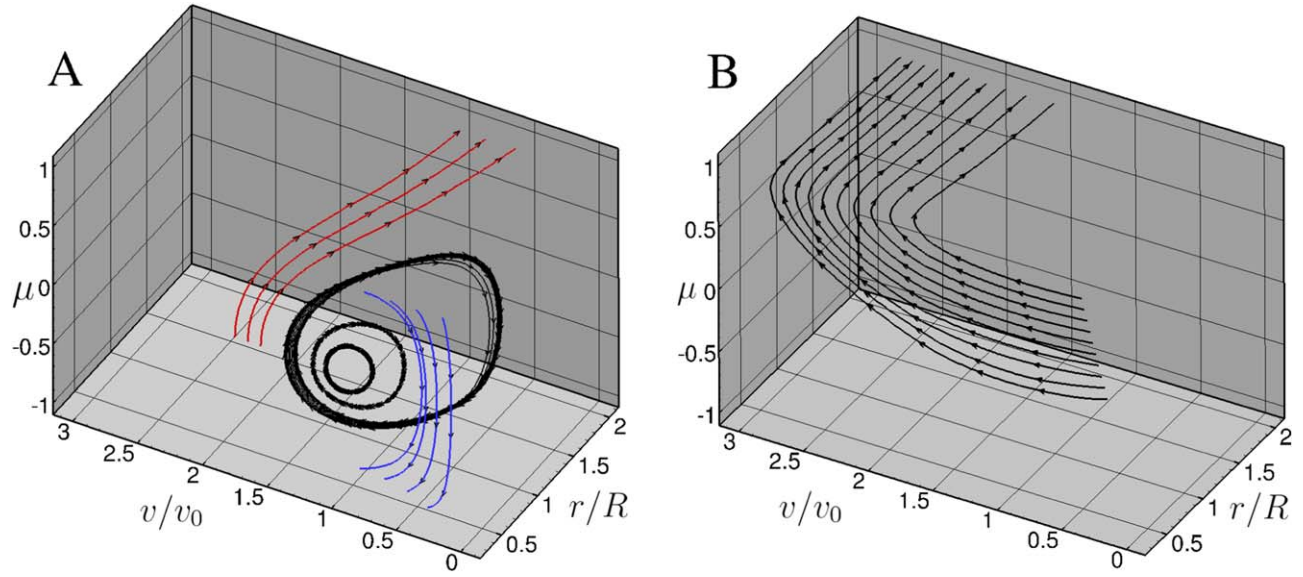

Figure 3. Examples of characteristics in the phase space (r, v, μ). (a) These curves are based on Equation (15), in which diffusion was ignored. The blue, red, and black characteristic lines correspond to ballistic, escaping, and trapped electrons, respectively (Lamy et al. 2003). (b) These curves are based on Equation (14), in which the term associated with diffusion in velocity space was included. $v_0 \approx 6 \times 10^8\,\mathrm{cm\,s^{-1}}$ is the velocity of particles with kinetic energy of 100 eV.

The equation of characteristics (14), without the term including f_r, can be rewritten as

$$\frac{dv}{dr} = -\frac{eE_\parallel}{mv}, \quad \frac{d\mu}{dr} = -\frac{eE_\parallel}{m}\frac{1-\mu^2}{v^2\mu} + \frac{1-\mu^2}{r\mu}. \tag{15}$$

Figure 3(a) illustrates the shape of the characteristics (15) in the phase space (r, v, μ). Three types of characteristics can be recognized, as is well known in exospheric models. The electrons with low energies (blue lines with black arrow) turn back to the Sun owing to reflection by the electric field. High-energy electrons can overcome the potential barrier and escape to interplanetary space, and they are represented by red lines with black arrows. The third group of characteristics corresponds to electrons trapped by the electric field from the far side and the magnetic bottle from the other side. Their characteristics are circles in the phase space, as can be seen by the black closed lines. The three groups of electrons are well known in kinetic exospheric models of the solar wind (Maksimovic et al. 1997; Lamy et al. 2003; Pierrard et al. 2011).

Figure 3(b) illustrates the effect of electron acceleration by whistler wave–particle interactions. It is clear that after including the term with f_r that is associated with acceleration, the characteristics are drastically modified and extend to great distances and never turn back, which means that all particles escape. For these characteristics that begin with smaller electron velocities, they are first energized to higher velocities before propagating far away. These characteristics correspond to the acceleration of electrons because Equation (14) is positive. Furthermore, electrons with the same kinetic energy but with a smaller pitch angle will be more strongly accelerated. Hence, diffusion in velocity space can initiate acceleration in phase space in the solar wind frame.

Our knowledge of the characteristics allows us to obtain an analytic solution of the kinetic equation. In the absence of $E_\parallel$ and whistler wave acceleration, the solution of Equation (13) is well known from molecular gas dynamics (Sone 2007):

$$f(r, v, \mu) = \begin{cases} g(v, \mu), & \sqrt{1-\left(\frac{r_L}{r}\right)^2} < \mu < 1 \\ 0. & -1 < \mu < \sqrt{1-\left(\frac{r_L}{r}\right)^2} \end{cases}, \tag{16}$$

for an arbitrary distribution $g(v, \mu)$ of particles injected at $r = r_L$. Figure 4 illustrates the effect of focusing by the diverging magnetic field for an initially half-Maxwellian distribution $g(v, \mu)$ based on the analytic solution (16) of gas dynamics. The injected particles can be any charged species and not necessarily electrons. In this example the left boundary from where the charged gas evaporates is chosen at $r_L = 0.1$ au. Although gas evaporation from a sphere is different from the transport of electrons in the solar wind, there are some interesting and useful similarities between them. It is seen that the VDF becomes highly anisotropic with increasing distance. The effect of focusing can also be seen from the graph of characteristics in Figure 3(a), where the red characteristics bend toward the top region where $\mu = 1$. Another thing to note is that the choice of left boundary r_L is arbitrary. Using a smaller left boundary r_L yields a stronger effect of focusing by the diverging magnetic field, and the VDF is narrower at 1 au. Third, for a half-Maxwellian distribution for the injected particles, the total, parallel, and perpendicular temperature decreases with increasing distance, as given by Sone & Sugimoto (1993),

$$\frac{T}{T_w} = 1 - \frac{2}{3\pi}\left[1 + \sqrt{1-\left(\frac{L}{r}\right)^2}\right]^2; \tag{17a}$$

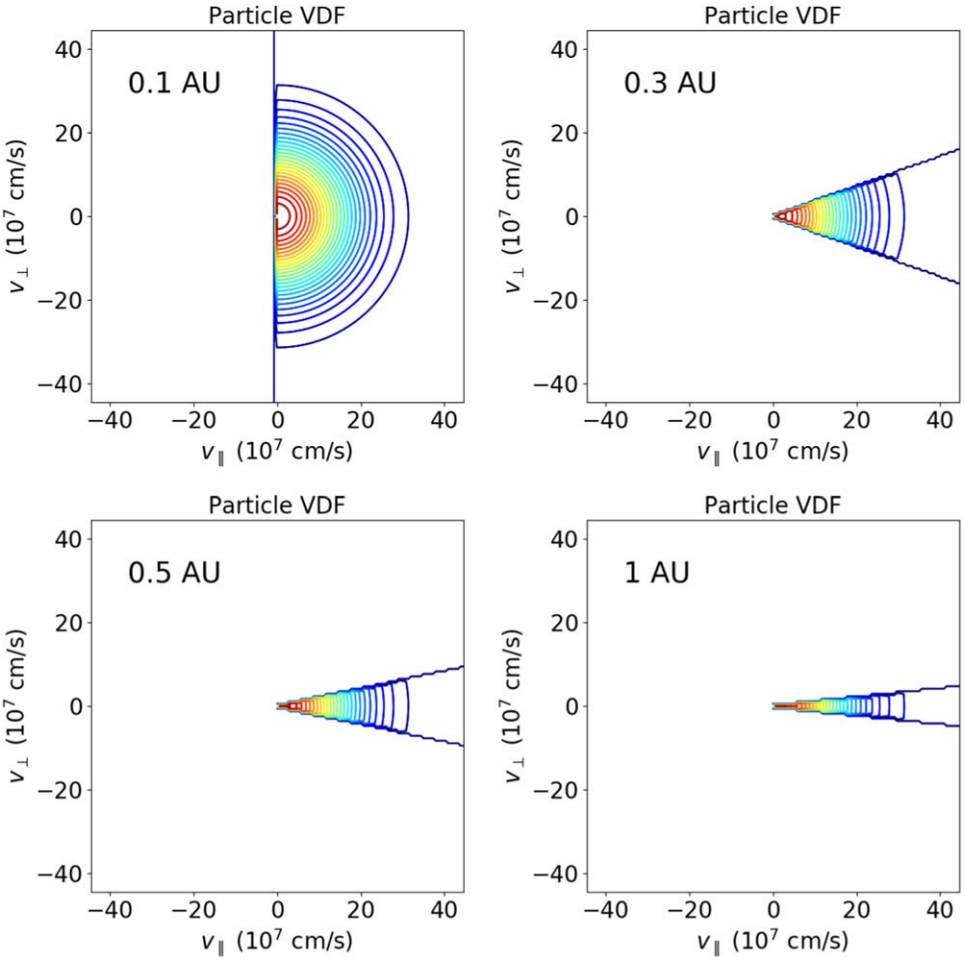

Figure 4. Effect of focusing with increasing radius for particle VDF. A half-Maxwellian VDF of any species of particles was injected at the left boundary $r_L = 0.1$ au.

$$\frac{T_\parallel}{T_w} = \left(1 - \frac{2}{\pi}\right)\left[1 + \sqrt{1 - \left(\frac{L}{r}\right)^2}\right]^2 - \sqrt{1 - \left(\frac{L}{r}\right)^2}; \quad (17b)$$

$$\frac{T_\perp}{T_w} = \frac{1}{2}\left[1 + \left(\frac{L}{r}\right)^2 - \sqrt{1 - \left(\frac{L}{r}\right)^2}\right], \quad (17c)$$

where L and T_w are the radius and temperature of the spherical condensed phase in which a steady flow evaporates, respectively. Fourth, for a kappa distribution of injected particles that has an enhanced high-energy tail with respect to a Maxwellian, the parallel temperature will increase with distance. This property is similar to the well-known velocity filtration effect of the exospheric model in the solar wind (Scudder 1992; Pierrard & Lemaire 1996; Maksimovic et al. 1997).

3. Numerical Results

3.1. Boundary Conditions

We solved numerically the Fokker–Planck kinetic Equation (13) for suprathermal electrons propagating in interplanetary space with appropriate boundary conditions. We assume that the electron VDF comprises two parts,

$$f_t = f_c + f_s, \quad (18)$$

where f_c is a Maxwellian core and f_s is a superimposed strahl. For now, we assume that the core is maintained as a Maxwellian via particle collisions and hence the distribution remains unchanged when core electrons propagate in interplanetary space. The Maxwellian core electron VDF is isotropic,

$$f_c(r, v) = n_c(r) 4\pi v^2 \left[\frac{m}{2\pi k_B T_c(r)}\right]^{3/2} \exp\left[-\frac{m}{2k_B T_c(r)} v^2\right], \quad (19)$$

where n_c and T_c are the number density and temperature, respectively, of the Maxwellian core electrons, which are defined according to Equations (8) and (9).

The numerical solutions of the kinetic transport Equation (13) yield the temporal and radial evolution of the function Y (hence the suprathermal electron VDF $f_s = Y/v^2 r^2$). At the inner boundary $r_L = 0.1$ au, a narrow cold beam that represents the suprathermal electron component is injected. The narrow beam has a drifting Maxwellian velocity distribution:

$$f_s(r = r_L, v, \mu) = n_{s0}\left(\frac{m}{2\pi k_B T_{s0}}\right)^{3/2} \times \exp\left[-\frac{mv^2(1-\mu^2)}{2k_B T_{s0}} - \frac{m(v\mu - v_d)^2}{2k_B T_{s0}}\right], \quad \mu > 0, \quad (20)$$

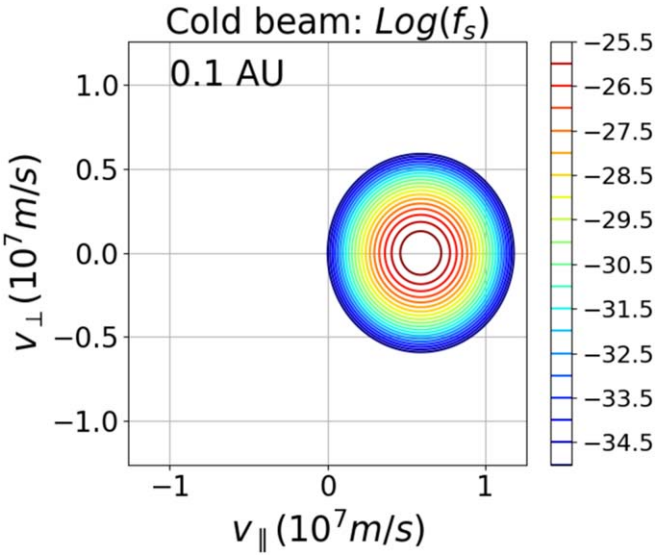

Figure 5. Contour levels of the injected cold beam at the left boundary $r_L = 0.1$ au.

where n_{s0} is the suprathermal electron number density at the inner boundary, v_d the drifting velocity along the magnetic field in the solar wind frame, and $T_{s0} \sim 5$ eV the temperature of the suprathermal electrons at the inner boundary. We choose the value of n_{s0} such that at 1 au the calculated number density of suprathermal electrons n_s is equal to about $1/20$ of that of the Maxwellian core electrons since observations show that the Maxwellian component composes about 95% of the total electron number density and the halo and strahl approximately 5%. The beam speed v_d was chosen so that the beam has a kinetic energy of 100 eV in the solar wind frame. Figure 5 shows the contour levels of the injected cold beam at the left boundary $r_L = 0.1$ au in the plane $(v_\parallel, v_\perp)$. The outer boundary condition at $r_\infty = 3$ is

$$f_s(r = r_\infty, v, \mu) = 0, \qquad \mu < 0, \tag{21}$$

which means no electrons entering from infinity. We prescribe the energy and angular distribution of electrons coming from the Sun ($\mu > 0$), and no electrons come from infinity. The energy and angular distribution of electrons returning back to the Sun ($\mu < 0$ at $r = r_0$) and escaping out to infinity ($\mu > 0$ at $r = r_\infty$) will be calculated by the code. These electrons include those reflected by the electric field and those produced with $\mu < 0$ owing to diffusion in μ.

As discussed above, we assume that the Maxwellian core electron VDF remains Mawellian at all heliocentric distances as the core electrons are transported in the solar wind. At a given heliocentric distance r_1, the Maxwellian core electron VDF is $f_c(r_1, v)$, and the suprathermal electron VDF $f_s(r_1, v, \mu)$ is the solution of the kinetic transport Equation (13) at the same heliocentric distance. The total electron VDF $f_t(r_1, v, \mu)$ at that heliocentric distance is then $f_c(r_1, v) + f_s(r_1, v, \mu)$.

3.2. Case 1

We begin by assuming the fixed fractional constant, choosing initially $f_r = 2.5 \times 10^{-5}$ in the kinetic transport Equation (13). We choose $f_r = 2.5 \times 10^{-5}$ to ensure that our results resemble those of observations. Figure 6 shows the solar wind electron VDF at 1 au. The Maxwellian core electron VDF f_c is directly obtained from Equation (19) by choosing $r = 1$ au, while the suprathermal electron VDF f_s $(r = 1, v)$ is obtained by integrating the calculated suprathermal electron VDF $f_s(r = 1, v, \mu)$ along μ, which is just the zero-order harmonic of the suprathermal electron VDF (see more details in Section 4).

Note that our calculation does not extend into the superhalo energy range; therefore, our solar wind electron VDF only includes the two components of a Maxwellian core and suprathermal electrons. Here the suprathermal electron distribution is now a combination of a halo and strahl. The observed solar wind electron VDF at 1 au over the full energy range is given by Figure 5 in Wang et al. (2012) and Figure 3 in Yoon et al. (2013), which were obtained from measurements made by the *WIND* spacecraft and the *STEREO A* and *B* spacecraft. Our constructed Figure 6 is very similar to their observed results in the energy range of the Maxwellian core and halo. This similarity of Figure 6 with the typical form of the observed electron VDF indicates that a cold beam of electrons can be scattered by wave–particle interaction due to whistler wave turbulence to form the observed distribution. By comparing our solar wind electron VDF with that shown in Figures 2 and 3 of Kim et al. (2015), we find that our simulated suprathermal electrons have a hotter temperature than their figures, which can be inferred by recognizing that our solar wind electron VDF (Figure 6) is wider than theirs shown in Figures 2 and 3 in the region $\sim 10^7$ m s^{-1}.

Figure 7 shows the contour levels of electron VDF in the plane $(v_\parallel, v_\perp)$ at different heliocentric distances separately. The total electron VDF is constructed by combining the Maxwellian core and the calculated suprathermal, $f_t(r, v, \mu) = f_c(r, v, \mu) + f_s(r, v, \mu)$. The injected suprathermal electron VDFs are fully pitch-angle scattered from a cold beam (see Equation (20)) and evolve gradually to a ring-shaped (or crescent-shaped) distribution by about 0.3 au, where the diffusion associated with whistler wave–particle interactions is strong. Some electrons are pitch-angle scattered into a sunward direction even at a distance of ~2–3 au. Since D_{vv} was included, the suprathermal electron VDF also diffuses in velocity space, and the suprathermal electron VDF broadens along v, i.e., suprathermal electrons are heated from a relative cold beam.

Figure 8 shows the radial evolution of parallel and perpendicular cuts of the solar wind electron VDF with respect to the interplanetary magnetic field from 0.1 to 3 au. Note that the parallel cut is along $v_\perp = 0$ and the perpendicular cut along $v_\parallel = 0$. Štverák et al. (2009) provide examples of the observed parallel cut of low-latitude solar wind electron VDFs from their fitting model for slow and fast solar wind, which used *Helios*, *Ulysses*, and *Cluster* observations (see Figures 6 and 10 in Štverák et al. 2009). The correspondence of Figure 8 with the observational Figures 6 and 10 of Štverák et al. (2009) is good and exhibits a similar radial variation. Sunward-propagating electrons are apparent as an enhancement in the $v_\parallel < 0$ region of the solar wind electron VDF. These sunward-propagating electrons can also be seen from Figure 7. These are not part of the Maxwellian core but were scattered from the outwardly propagating strahl by wave–particle interactions. The emergence of these sunward-propagating electrons demonstrates the effectiveness of whistler wave–particle interactions in scattering a highly anisotropic field-aligned cold beam into an almost

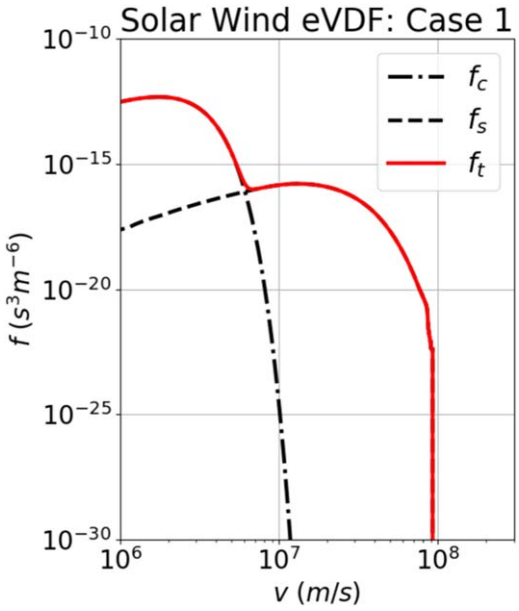

Figure 6. Theoretical construction of the solar wind electron VDF $f_t = f_c + f_s$ at 1 au for case 1 with a fraction constant $f_r = 2.5 \times 10^{-5}$. f_c is given by Equation (19) at $r = 1$ au, and $f_s(r = 1, v)$ is obtained by integrating the suprathermal electron VDF $f_s(r = 1, v, \mu)$ calculated from Equation (13) along μ.

isotropic distribution, as illustrated by the antisunward direction energetic electrons. The parallel cut solar wind electron VDF is asymmetric. Although the highly anisotropic field-aligned cold beam is scattered into an almost isotropic distribution, there is an imbalance between antisunward- and sunward-propagating electrons. Since the suprathermal electrons streaming in the antisunward direction are still field aligned, they can be regarded as part of the strahl.

3.3. Case 2

From the previous case we find that the calculated suprathermal electron temperature is higher than that typically observed (Figure 5 in Wang et al. 2012 and Figure 3 in Yoon et al. 2013). To reduce the suprathermal electron temperature, we choose a smaller fractional constant to reduce the diffusion coefficients by assuming $f_r = 1 \times 10^{-5}$.

Figure 9 shows the solar wind electron VDF at 1 au. The suprathermal electron temperature was reduced as expected. The combined total solar wind electron VDF resembles those typically observed (Figure 5 in Wang et al. 2012 and Figure 3 in Yoon et al. 2013) in the vicinity of 10^7 m s^{-1}. However, using a smaller fractional constant results in diffusion coefficients that are too small since whistler wave–particle scattering is not strong enough to scatter many electrons in the highly anisotropic field-aligned cold beam into the sunward direction. Figure 10 illustrates the contour level of the electron VDF in the plane ($v_\parallel$, $v_\perp$), and Figure 11 shows the radial evolution of a cut of the solar wind electron VDF parallel and perpendicular to the interplanetary magnetic field from 0.1 to 3 au. In this case, there are far fewer sunward-propagating electrons, meaning that the scattering of suprathermal electrons is not sufficiently effective, which is no surprise because in this case the fractional constant was reduced and hence the corresponding whistler wave–particle interactions are weaker. Furthermore, the suprathermal electron VDF does not broaden compared to that of case 1 because diffusion in velocity space is reduced in this case.

4. Discussion

Since we have obtained the full VDF of the suprathermal electrons, we may exploit $\mu \in [-1, 1]$ and expand the calculated $f(r, v, \mu, t)$ in an infinite series of Legendre polynomials $P_n(\mu)$ (Zank 2014),

$$f(r, v, \mu, t) = \frac{1}{2}\sum_{n=0}^{\infty}(2n + 1)P_n(\mu)f_n(r, v, t). \tag{22}$$

where $f_n(r, v, t)$ is the nth harmonic of the distribution function

$$f_n(r, v, t) = 2\pi\int_{-1}^{1} P_n(\mu)f(r, v, \mu, t)d\mu \tag{23}$$

and

$$P_0(\mu) = 1; \quad P_1(\mu) = \mu; \quad P_2(\mu) = \frac{1}{2}(3\mu^2 - 1); \cdots$$

are the first three Legendre polynomials. We can calculate the differential anisotropy ξ of the suprathermal electrons from the first harmonics by using the method given by Gleeson & Axford (1967),

$$\xi = \frac{f_1}{f_0}. \tag{24}$$

Figure 12 shows the differential anisotropy ξ of the suprathermal electrons at different locations from 0.1 to 3 au. In general, the differential anisotropy increases with increasing distance and electron kinetic energy, tending to $\xi \sim 0.8$ as both increase. Besides the differential anisotropy, we also obtain the pitch-angle distributions (PADs) of the calculated suprathermal electron VDF, which are shown in Figure 13.

From Figures 12 and 13, it is apparent that the suprathermal electron VDF at a smaller distance is more isotropic than that at a larger distance. The cold beam injected at the inner boundary is initially highly field aligned and is significantly scattered by whistler waves at smaller distances. As the distance increases, the scattering of electrons by whistler waves is less effective (see Figure 2). Hence, at larger distances the suprathermal electrons are not scattered by whistler waves sufficiently to maintain quasi-isotropy, and their VDFs become anisotropic again.

By using the derived total solar wind electron VDF ($f_t = f_c + f_s$), we can calculate the radial variation of various parameters (such as the suprathermal electron temperature and heat flux) by taking moments of the solar wind electron VDF. Specifically, the methods to calculate the first few orders of moments of a electron VDF are given in Pierrard (2012) and Pierrard et al. (2016). The number density of the supathermal electrons is

$$n_s(r) = \int f(r, v, \mu)d\boldsymbol{v}, \tag{25}$$

where $d\boldsymbol{v} = 2\pi v^2 dv d\mu$ corresponds to assuming gyrotropy.

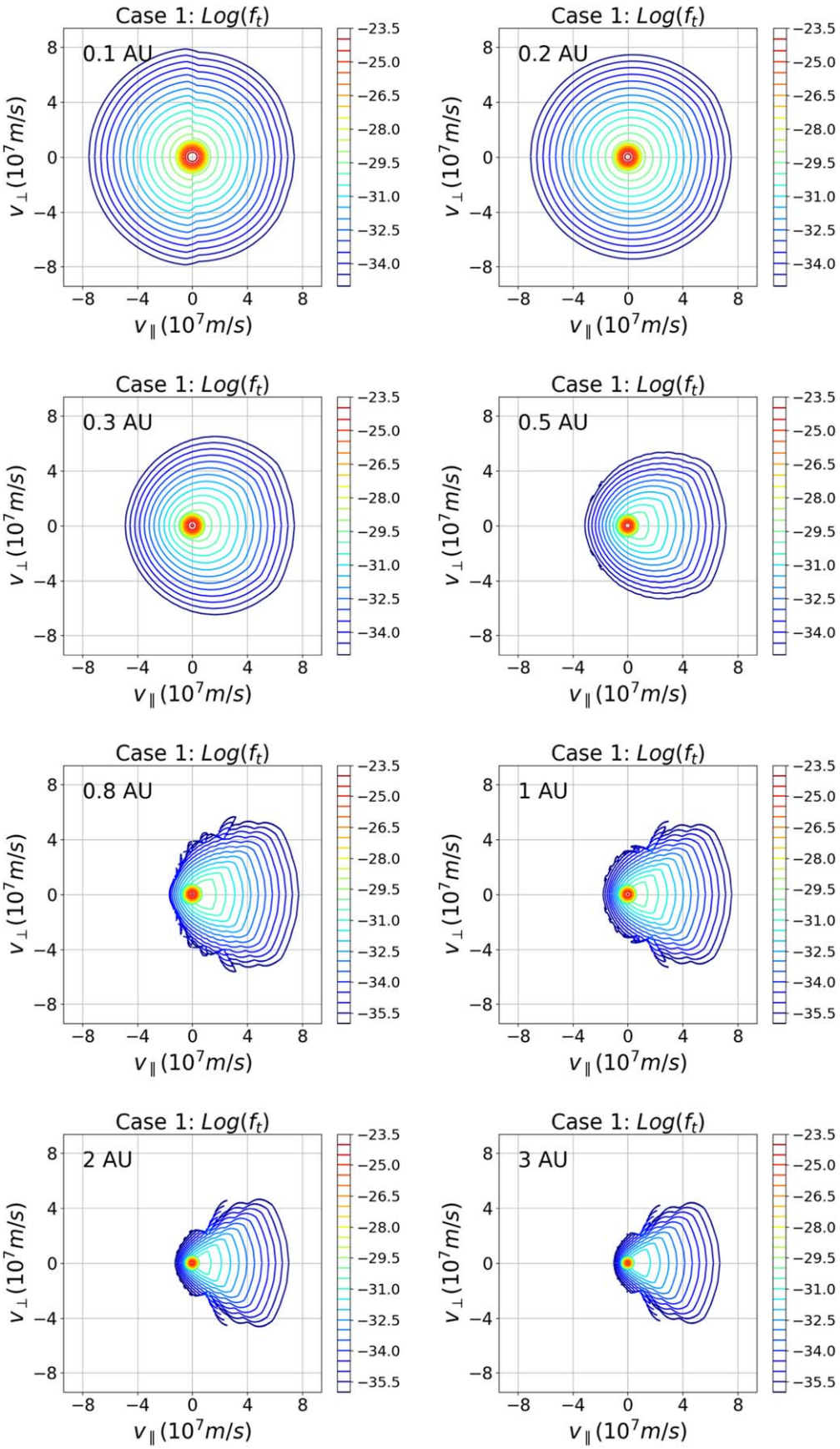

Figure 7. Contour levels of the total electron VDF from 0.1 to 3 au in case 1, where the fractional constant is chosen as $f_r = 2.5 \times 10^{-5}$ in the kinetic transport Equation (13). The total electron VDF is constructed by combining the Maxwellian core and the calculated suprathermal, $f_t(r, v, \mu) = f_c(r, v, \mu) + f_s(r, v, \mu)$.

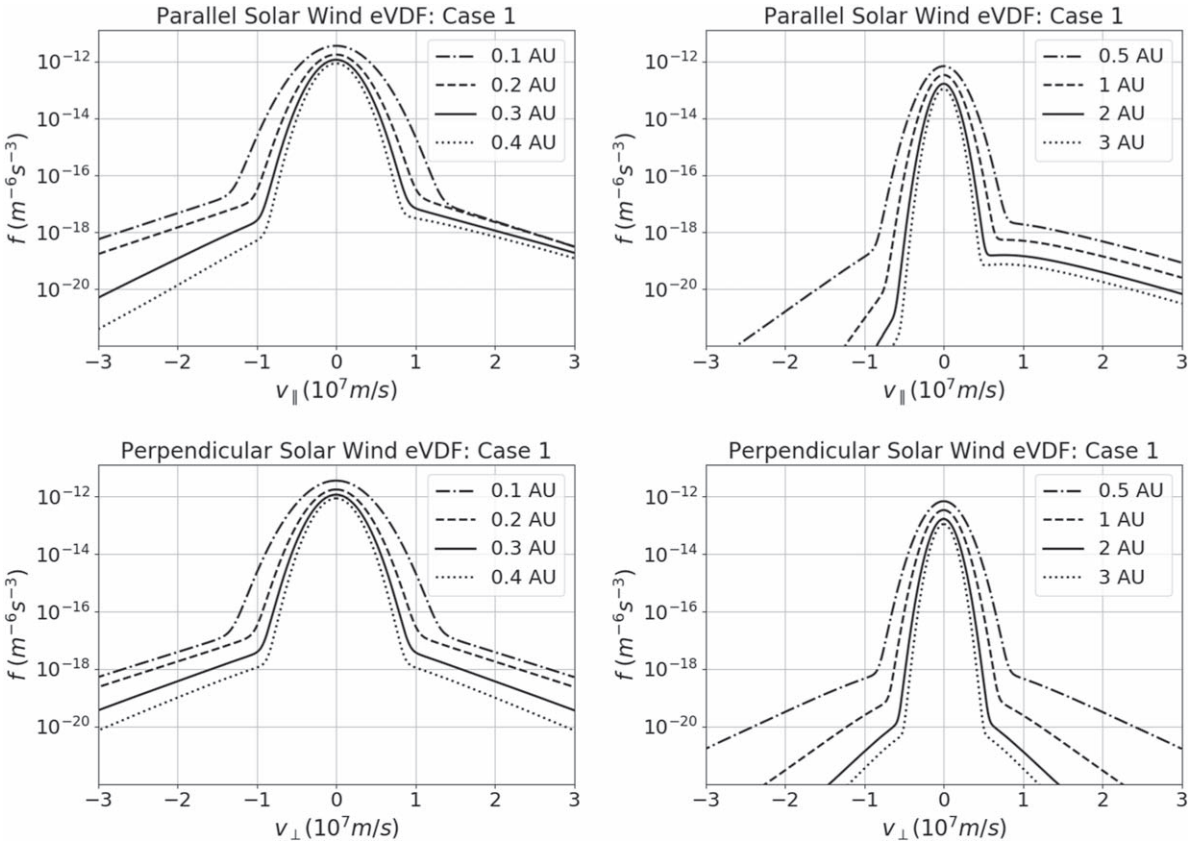

Figure 8. Radial evolution of cuts through the solar wind electron VDF in a direction parallel and perpendicular to the interplanetary magnetic field in case 1.

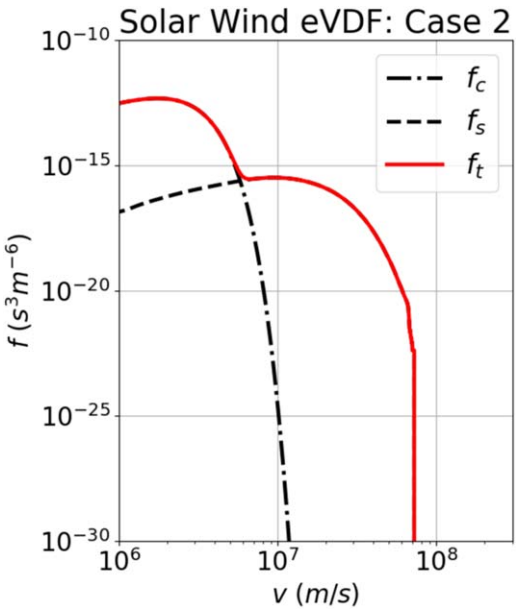

Figure 9. Theoretical construction of the solar wind electron VDF $f_t = f_c + f_s$ at 1 au for case 2 with a fraction constant $f_r = 1 \times 10^{-5}$. f_c is given by Equation (19) at $r = 1$ au, and f_s $(r = 1,\ v)$ is obtained by integrating the suprathermal electron VDF $f_s(r = 1, v, \mu)$ calculated from Equation (13) along μ.

The parallel particle flux of the suprathermal electrons corresponds to the first-order moment,

$$F_s(r) = \int v_\parallel f(r,\ v,\ \mu) d\boldsymbol{v}. \tag{26}$$

The suprathermal electron bulk velocity is the ratio of particle flux to the number density,

$$u_s(r) = \frac{F_s(r)}{n_s(r)}. \tag{27}$$

The second-order moment of the suprathermal electron VDF yields the temperature components of the suprathermal electrons,

$$T_{s\parallel}(r) = \frac{m}{n_s k_B} \int v_\parallel^2 f(r,\ v,\ \mu) d\boldsymbol{v}; \tag{28}$$

$$T_{s\perp}(r) = \frac{m}{n_s k_B} \int v_\perp^2 f(r,\ v,\ \mu) d\boldsymbol{v}, \tag{29}$$

where k_B is the Boltzmann constant. The average or total temperature of the suprathermal electrons is given by

$$T_s(r) = \frac{1}{3}[T_{\parallel s}(r) + 2T_{\perp s}(r)]. \tag{30}$$

The third-order moment of the suprathermal electron VDF yields the heat flux components parallel and perpendicular to the magnetic field,

$$q_\parallel(r) = m \int (v_\parallel - u)^3 f(r,\ v,\ \mu) d\boldsymbol{v}; \tag{31}$$

$$q_\perp(r) = \frac{1}{2} m \int v_\perp^2 (v_\parallel - u) f(r,\ v,\ \mu) d\boldsymbol{v}. \tag{32}$$

Note that the heat fluxes for the suprathermal electrons are actually that of the total electron distribution, since we assume in the present paper that the total electron VDF is a

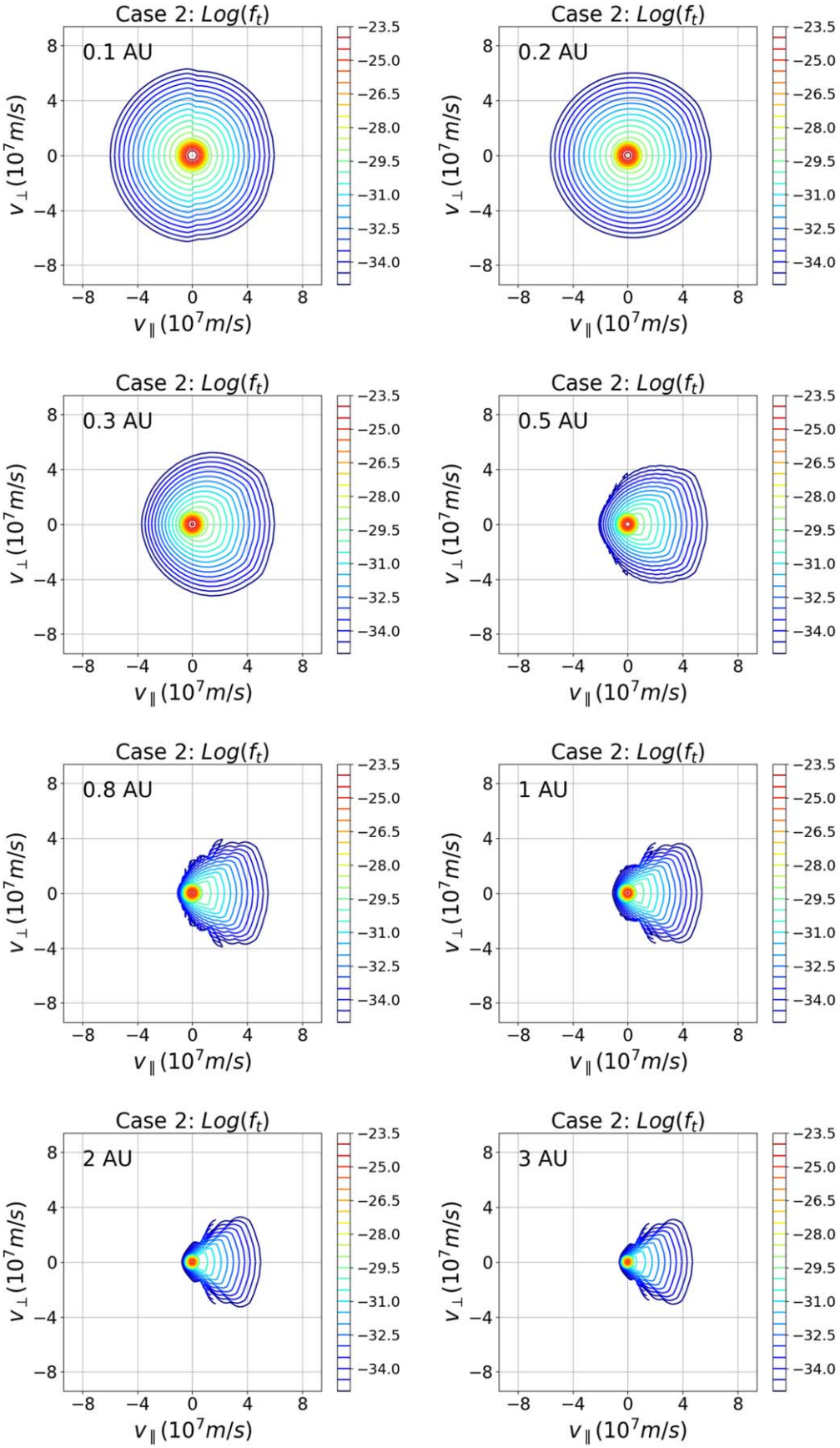

Figure 10. Contour levels of the total electron VDF from 0.1 to 3 au in case 2, where the fractional constant is chosen as $f_r = 1 \times 10^{-5}$ in the kinetic transport Equation (13).

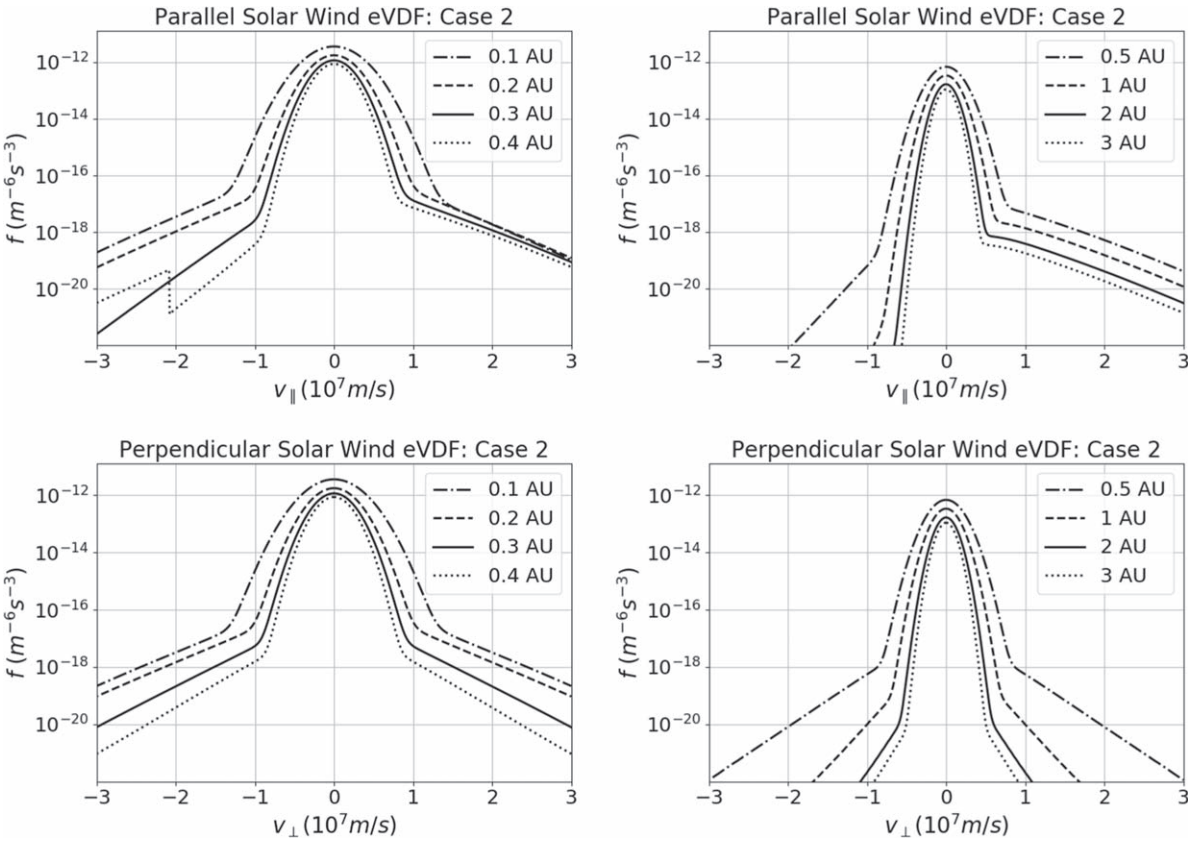

Figure 11. Radial evolution of cuts through the solar wind electron VDF in a direction parallel and perpendicular to the interplanetary magnetic field in case 2.

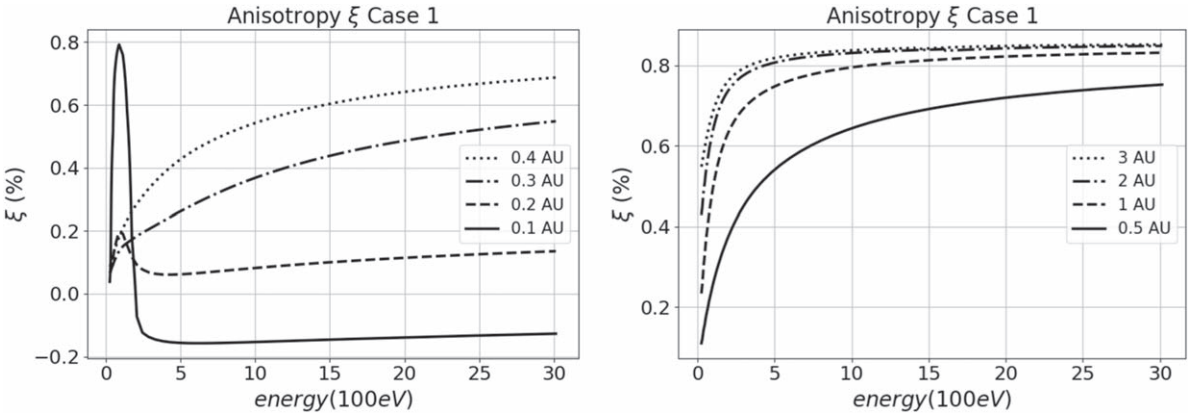

Figure 12. Differential anisotropy of suprathermal electrons as a function of kinetic energy at different positions from 0.1 to 3 au.

combination of the Maxwellian core and the suprathermal electrons, and the heat flux of the Maxwellian core electron VDF is zero. The average or total heat flux of the suprathermal electrons is given by

$$q_t(r) = \frac{1}{3}[q_\parallel(r) + 2q_\perp(r)]. \quad (33)$$

Figure 14 shows the radial variation of the electron number density and bulk velocity. Parameter n_c is the number density of the background Maxwellian core electrons, which is given by Equation (8), and n_s refers to the suprathermal electrons. The core number density n_c is much larger than n_s, and the total electron number density $n_e = n_c + n_s$ is essentially n_c. At 1 au, n_s is about 20 times smaller than n_c, which is consistent with observations. The bulk velocity of a Maxwellian distribution in the solar wind frame is zero, so the bulk velocity of suprathermal electron u_s is also that of the total electrons.

In the left panel of Figure 15, the black line shows the calculated suprathermal electron temperature T_s as a function of distance. It is clear that T_s increases slightly with heliocentric distance, which is consistent with observations from Pierrard et al. (2016). Our derived temperature is a little higher than shown in Figure 1(b) of Pierrard et al. (2016). The blue dashed line indicates the temperature of the Maxwellian core T_c as given by Equation (9), i.e., the assumed background temperature. T_s is one order of magnitude larger than T_c. The right panel shows the radial variation for the temperature anisotropy of suprathermal electrons ($A = T_\perp/T_\parallel$). No anisotropy

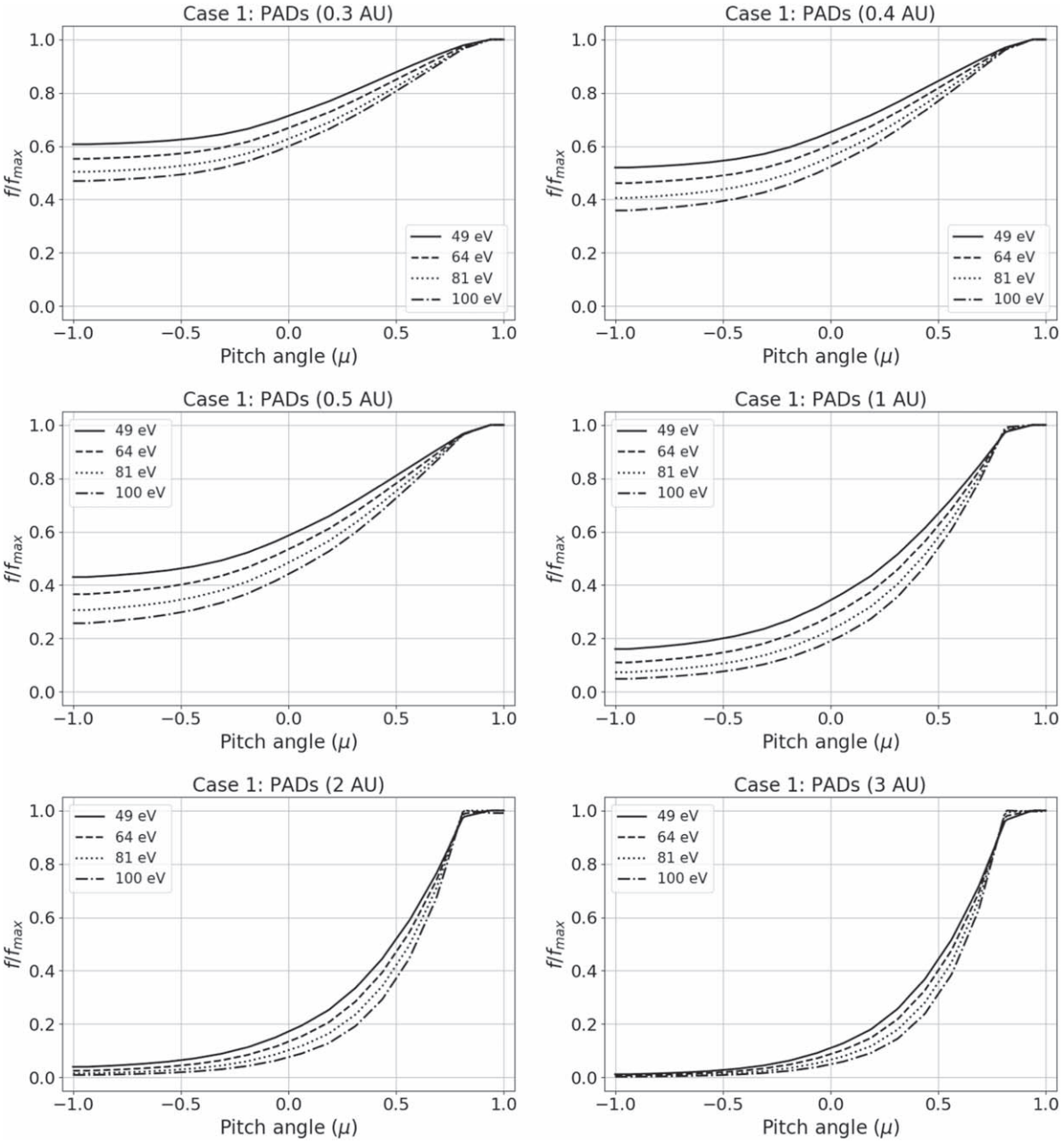

Figure 13. PADs of the calculated suprathermal electron VDF at 0.3, 0.4, 0.5, 1, 2, and 3 au.

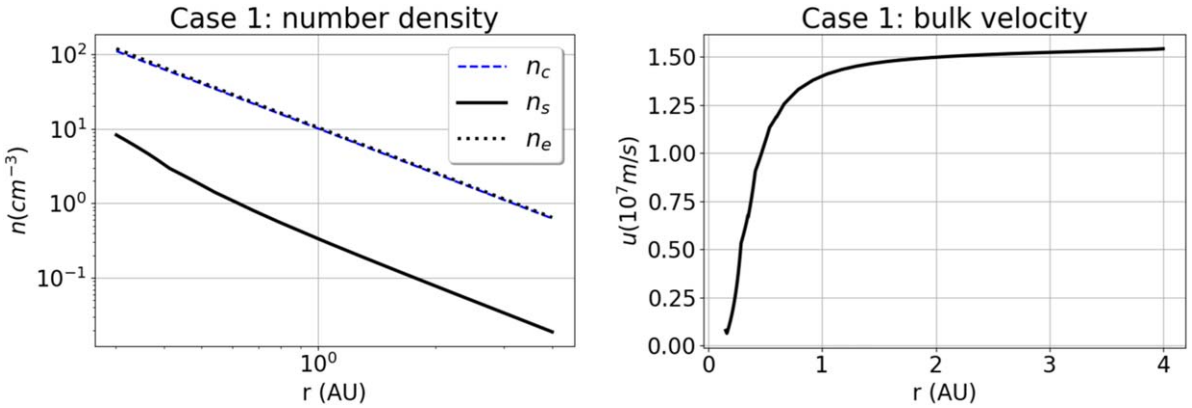

Figure 14. Left: number density of the Maxwellian core electrons (blue dashed line) and suprathermal electrons (black solid line). Right: radial variation of the bulk velocity of suprathermal electrons.

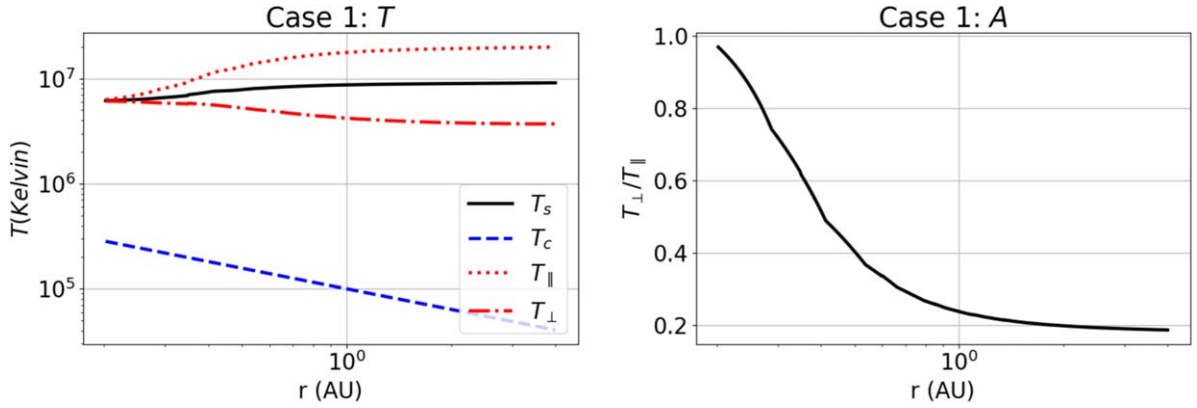

Figure 15. Left: electron temperature vs. distance. The black solid line T_s, red dotted line $T_\parallel$, and red dashed–dotted line $T_\perp$ are derived from the suprathermal electron VDF by Equation (33), while the blue dashed line T_c is the temperature of the background Maxwellian core given by Equation (9). Right: radial variation of the temperature anisotropy $A = T_\perp/T_\parallel$.

corresponds to $A = 1$ and high anisotropy to $A \to 0$.[5] The radial variation of A indicates that the suprathermal electron temperature becomes more anisotropic with heliocentric distance, which is consistent with the previous result showing the differential anisotropy ξ in the electron VDF (Figure 12).

Another parameter of great interest that can be obtained from the calculated suprathermal electron VDF is the solar wind heat flux. Since the total solar wind VDF is composed of two parts, the Maxwellian core and the scattered suprathermal parts, the heat flux of the Maxwellian is zero, and so the solar wind electron heat flux is only that of the calculated suprathermal component. Figure 16 shows the radial variation of the solar wind electron heat flux from about 0.4 to 4 au. We find that the total and component heat fluxes decrease as $\propto 1/r^{2.3}$. The index depends on the location of the inner boundary and the diffusion coefficients. Scime et al. (2001) found that the average heat flux varies as $q_e \propto r^{-2.9}$ from *Ulysses* observations. In our calculation, if the location of the inner boundary was chosen at 0.3 au with a fraction constant $f_r = 5 \times 10^{-5}$, then the total and component heat fluxes vary as $\propto r^{-2.9}$, suggesting that stronger whistler wave–particle interactions result in a steeper radial profile of heat flux.

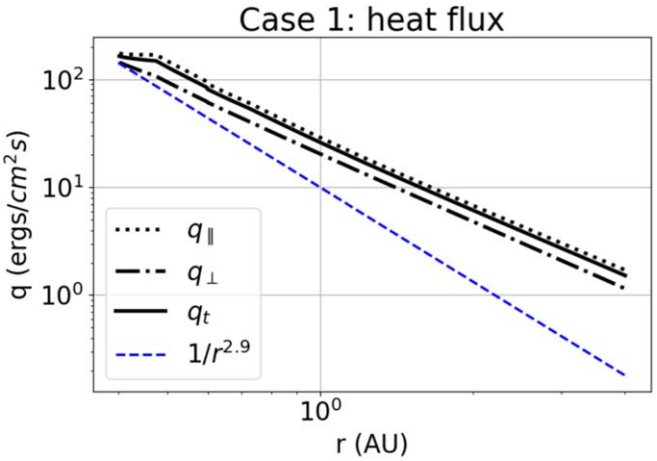

Figure 16. Radial variation of the total q_t, parallel $q_\parallel$, and perpendicular $q_\perp$ heat fluxes from about 0.4 to 4 au. The blue dashed line shows $q \propto r^{-2.9}$, which is obtained from *Ulysses* observations by Scime et al. (2001).

5. Summary and Conclusion

We have developed an efficient method for solving the Fokker–Planck kinetic equation for electrons in the solar wind in the presence of whistler wave–particle interactions. This is a first step toward a kinetic model of the solar wind plasma, which requires combining electron and ion kinetics with a self-consistent calculation of the electric field. In the present paper, we restricted our attention to the suprathermal electron energy range and neglected those energies corresponding to the superhalo. We assumed that the solar wind electron VDF was composed of two components: a Maxwellian core and suprathermal electrons. Unlike the Maxwellian core, suprathermal electrons are subject to scattering by whistler wave turbulence. By assuming an expanding background of constant velocity radial flow and radial magnetic field and choosing appropriate diffusion coefficients in which the off-diagonal terms in the diffusion tensor were ignored, we obtained a kinetic equation for the suprathermal electrons that describes their spatial and temporal evolution in the solar wind. By solving this kinetic transport equation, we can follow the transport of the suprathermal electrons and hence the spatial variation of the solar wind electron VDF. Our numerical method solves the Fokker–Planck kinetic transport equation using a finite-volume method with adaptive Cartesian mesh, without splitting physical and velocity space. We have shown that in the absence of diffusion the particles move along the characteristics in the phase space (r, v, μ), and the electron VDF is quickly focused into a narrow strahl because of the radial magnetic fields. However, wave–particle interactions due to whistler wave turbulence reduce the focusing effect of the radial magnetic field, playing an important role in the formation of the solar wind electron VDF.

A highly field-aligned cold beam of electrons is chosen to represent the suprathermal electrons that we inject at the inner boundary. The suprathermal electrons scatter via wave–particle interactions induced by whistler wave turbulence. Our results are summarized as follows:

[5] The differential anisotropy ξ measures the departure of the distribution function from isotropy (the zeroth-order term in the Lagrange polynomial representation of the suprathermal electron distribution function), and the f_1 component is a measure of the heat flux. The heat flux from the isotropic component f_0 is zero. However, the parallel and perpendicular temperature moments both include the f_0 contribution. $T_\parallel \propto \int v_\parallel^2 (f_0 + \mu f_1) d\boldsymbol{v} = T + \int v_\parallel^2 \mu f_1 d\boldsymbol{v}$ and $T_\perp \propto \int v_\perp^2 (f_0 + \mu f_1) d\boldsymbol{v} = T + \int v_\perp^2 \mu f_1 d\boldsymbol{v}$, where T is the temperature corresponding to the zeroth-order Lagrange polynomial. Hence, when $f_1 = 0$, the differential anisotropy $\xi = 0$, but $A = T_\perp/T_\parallel = (T + 0)/(T + 0) = 1$.

1. The solar wind electron VDFs as a combination of a Maxwellian core and the calculated suprathermal component at 1 au are constructed, i.e., Figures 6 and 9. In the energy range of the Maxwellian core, halo, and strahl, our total electron VDFs resemble the results of Kim et al. (2015). Since our total electron VDF does not include superhalo electrons, Figures 6 and 9 do not extend to electron velocities $\geqslant 10^8$ m s^{-1}.
2. The radial variation of the total electron VDF in the plane ($v_{\parallel}$, $v_{\perp}$) and the parallel and perpendicular cuts of the total electron VDF for two cases over a range from 0.1 to 3 au are obtained and shown in Figures 7, 8, 10, and 11.
3. The differential anisotropy (ξ) and the PADs of the suprathermal electrons at different heliocentric distances for case 1 are calculated and plotted in Figures 12 and 13. The figures show that the suprathermal electron VDF at a smaller distance is more isotropic than that at a larger distance. The cold beam injected at the inner boundary is initially highly field aligned and is significantly scattered by whistler waves at smaller distances. As the distance increases, the scattering of electrons by whistler waves is less effective. Hence, at larger distances the suprathermal electrons are not scattered by whistler waves sufficiently to maintain quasi-isotropy, and their VDFs become anisotropic again.
4. The radial variation of the electron number density (n_c, n_s, and n_e) and the electron bulk speed (u) in the solar wind frame are shown in Figure 14. At 1 au, n_s is about 20 times smaller than n_c, which is consistent with observations.
5. The radial variation of the electron temperature (T_c, T_c, $T_{\parallel}$, and $T_{\perp}$) and the temperature anisotropy A are shown in Figure 15. We find that the suprathermal electron temperature T_c slightly increases with the heliocentric distance, which is consistent with the observations shown Pierrard et al. (2016).
6. The radial variation of the electron heat fluxes (q_t, $q_{\parallel}$ and $q_{\perp}$) is shown in Figure 16. We find that the electron heat fluxes decrease as $\propto 1/r^{2.3}$. The index depends on the location of the inner boundary and the diffusion coefficients.

Our results confirm that whistler wave turbulence can scatter a highly anisotropic cold beam into a nearly isotropic distribution with a substantial number of sunward-propagating electrons. Nonetheless, there remain more antisunward electrons than sunward ones. The combination of these results can be interpreted as the formation and evolution of the halo and strahl, which is consistent with the most widely accepted assumption that halo electrons are pitch-angle scattered from strahl electrons as they propagate in interplanetary space. The electron VDF at 1 au and the radial variation of the parallel cut of the electron VDF with respect to the interplanetary magnetic field are similar to multiple observations (Wang et al. 2012; Kim et al. 2015; Stverák et al. 2015). The temperature of suprathermal electrons T_s increases slightly with heliocentric distance, which is consistent with the observations from Pierrard et al. (2016). The similarity between our results and observations validates our assumptions and the numerical transport method.

In the present paper, the off-diagonal terms in the diffusion coefficients (5) are ignored in the kinetic transport Equation (12) since the diffusion is dominated by diagonal terms. However, Figure 2 shows that the off-diagonal terms $D_{v\mu}$ and $D_{\mu v}$, although they are about five times smaller than $D_{\mu\mu}$, are still larger than D_{vv}. The off-diagonal terms will likely play an important role in both pitch-angle scattering and velocity diffusion of suprathermal electrons. Our preliminary calculation with a full diffusion tensor shows that the off-diagonal terms $D_{v\mu}$ and $D_{\mu v}$ introduce a form of "advection" of the distribution function in the (v, μ) plane. As a result, diffusion in the (v, μ) plane at the same heliocentric distances is slightly suppressed. An expanded version of the diffusion solver in Basilisk that will solve a full diffusion tensor with both diagonal and off-diagonal terms is under development, and this will be presented in a following paper.

This work was partially supported by the NSF EPSCoR project OIA-1655280 "Connecting the Plasma Universe to Plasma Technology in AL: The Science and Technology of Low-Temperature Plasma." B.T. acknowledges the support of a NASA Earth and Space Science Fellowship Program grant HELIO19R-0001.

ORCID iDs

Bofeng Tang https://orcid.org/0000-0002-2261-6629
Gary P. Zank https://orcid.org/0000-0002-4642-6192

References

Adhikari, L., Zank, G., Hunana, P., et al. 2017, ApJ, 841, 85
Anderson, B., Skoug, R., Steinberg, J., & McComas, D. 2012, JGRA, 117, A04107
Arslanbekov, R. R., Kolobov, V. I., & Frolova, A. A. 2013, PhRvE, 88, 063301
Boldyrev, S., & Horaites, K. 2019, MNRAS, 489, 3412
Che, H., & Goldstein, M. 2014, ApJL, 795, L38
Chen, W., Lai, C., Lin, H., & Lin, W. 1972, JGR, 77, 1
Ergun, R., Larson, D., Lin, R., et al. 1998, ApJ, 503, 435
Feldman, W., Asbridge, J., Bame, S., & Montgomery, M. 1974, RvGeo, 12, 715
Feldman, W., Asbridge, J., Bame, S., Montgomery, M., & Gary, S. 1975, JGR, 80, 4181
Fujimoto, K., & Sydora, R. D. 2008, GeoRL, 35, L19112
Gleeson, L., & Axford, W. 1967, ApJL, 149, L115
Graham, G., Rae, I., Owen, C., et al. 2017, JGRA, 122, 3858
Gurgiolo, C., Goldstein, M., Viñas, A., & Fazakerley, A. 2012, AnGeo, 30, 163
Gurgiolo, C., & Goldstein, M. L. 2016, AnGeo, 34, 1175
Hammond, C., Feldman, W., McComas, D., Phillips, J., & Forsyth, R. 1996, A&A, 316, 350
Horaites, K., Boldyrev, S., Krasheninnikov, S., et al. 2015, PhRvL, 114, 245003
Horaites, K., Boldyrev, S., & Medvedev, M. V. 2018, MNRAS, 484, 2474
Horaites, K., Boldyrev, S., Wilson, L. B., III, Viñas, A. F., & Merka, J. 2017, MNRAS, 474, 115
Isenberg, P. A. 1997, JGR, 102, 4719
Kim, S., Yoon, P. H., Choe, G., & Wang, L. 2015, ApJ, 806, 32
Kolobov, V., & Arslanbekov, R. 2012, JCoPh, 231, 839
Kolobov, V., Arslanbekov, R., & Levko, D. 2019, in AIP Conf. Proc. 2132, 31ST INTERNATIONAL SYMPOSIUM ON RAREFIED GAS DYNAMICS: RGD31, ed. Y. Zhang et al. (Melville, NY: AIP), 060011
Kolobov, V., & Godyak, V. 2019, PhPl, 26, 060601
Kolobov, V. I. 2003, ComMS, 28, 302
Kolobov, V. I. 2013, PhPl, 20, 101610
Lamy, H., Pierrard, V., Maksimovic, M., & Lemaire, J. 2003, JGRA, 108, 1047
Landi, S., Matteini, L., & Pantellini, F. 2012, ApJ, 760, 143
Lazar, M., Pierrard, V., Shaaban, S., Fichtner, H., & Poedts, S. 2017, A&A, 602, A44
Lazar, M., Poedts, S., Schlickeiser, R., & Dumitrache, C. 2014, MNRAS, 446, 3022
Lemons, D. S., & Feldman, W. C. 1983, JGR, 88, 6881
Lie-Svendsen, Ø, Hansteen, V. H., & Leer, E. 1997, JGR, 102, 4701

Lie-Svendsen, Ø, & Leer, E. 2000, JGR, 105, 35
Lie-Svendsen, Ø, & Rees, M. 1996, JGR, 101, 2415
Maksimovic, M., Pierrard, V., & Lemaire, J. 1997, A&A, 324, 725
Maksimovic, M., Zouganelis, I., Chaufray, J.-Y., et al. 2005, JGRA, 110, A09104
Marsch, E., Mühlhäuser, K.-H., Schwenn, R., et al. 1982, JGR, 87, 52
Pagel, C., Gary, S. P., De Koning, C. A., Skoug, R. M., & Steinberg, J. T. 2007, JGRA, 112, A04103
Pierrard, V. 2012, SSRv, 172, 315
Pierrard, V., & Lazar, M. 2010, SoPh, 267, 153
Pierrard, V., Lazar, M., Poedts, S., et al. 2016, SoPh, 291, 2165
Pierrard, V., Lazar, M., & Schlickeiser, R. 2011, SoPh, 269, 421
Pierrard, V., & Lemaire, J. 1996, JGR, 101, 7923
Pierrard, V., Maksimovic, M., & Lemaire, J. 1999, JGR, 104, 17021
Pierrard, V., Maksimovic, M., & Lemaire, J. 2001, JGR, 106, 29305
Pilipp, W., Miggenrieder, H., Montgomery, M., et al. 1987a, JGR, 92, 1075
Pilipp, W., Miggenrieder, H., Montgomery, M., et al. 1987b, JGR, 92, 1093
Salem, C. 2000, PhD dissertation, Univ. Paris
Salem, C., Hubert, D., Lacombe, C., et al. 2003, ApJ, 585, 1147
Schlickeiser, R. 1989, ApJ, 336, 243
Scime, E. E., Littleton, J., Gary, S. P., Skoug, R., & Lin, N. 2001, GeoRL, 28, 2169
Scudder, J. D. 1992, ApJ, 398, 299
Shalchi, A. 2011, ApJ, 728, 113
Skilling, J. 1971, ApJ, 170, 265
Sone, Y. 2007, Molecular Gas Dynamics: Theory, Techniques, and Applications (New York: Springer Science Business Media)
Sone, Y., & Sugimoto, H. 1993, PhFlA, 5, 1491
Steinacker, J., & Miller, J. A. 1992, ApJ, 393, 764
Štverák, Š, Maksimovic, M., Trávníček, P. M., et al. 2009, JGRA, 114, A05104
Štverák, Š, Trávníček, P., Maksimovic, M., et al. 2008, JGRA, 113, A03103
Stverák, S. t., Trávníček, P. M., & Hellinger, P. 2015, JGRA, 120, 8177
Tang, B., Zank, G. P., & Kolobov, V. 2018, JPhCS, 1100, 012025
Tao, J., Wang, L., Zong, Q., et al. 2016, ApJ, 820, 22
Tong, Y., Vasko, I. Y., Artemyev, A. V., Bale, S. D., & Mozer, F. S. 2019, ApJ, 878, 41
Vocks, C., & Mann, G. 2003, ApJ, 593, 1134
Vocks, C., Mann, G., & Rausche, G. 2008, A&A, 480, 527
Vocks, C., Salem, C., Lin, R., & Mann, G. 2005, ApJ, 627, 540
Wang, L., Lin, R. P., Salem, C., et al. 2012, ApJL, 753, L23
Weber, E. J., & Davis, L., Jr 1967, ApJ, 148, 217
Wei, X., Cao, J., Zhou, G., et al. 2007, JGRA, 112, A10225
Yoon, P. 2015, JPhCS, 642, 012030
Yoon, P. H., Kim, S., & Choe, G. 2015, ApJ, 812, 169
Yoon, P. H., Ziebell, L. F., Gaelzer, R., Wang, L., & Lin, R. P. 2013, Terr. Atmos. Oceanic Sci., 24, 175
Zabelok, S., Arslanbekov, R., & Kolobov, V. 2015, JCoPh, 303, 455
Zank, G. P. 2014, LNP, 877